Fall 10-2011

ISOTOPE IDENTIFICATION AND SOURCE DIRECTIONAL DETERMINATION USING GAMMA RADIATION PROFILING

Christopher L. Schrage

University of Nebraska – Lincoln, flux2002@aol.com

ISOTOPE IDENTIFICATION AND SOURCE DIRECTIONAL DETERMINATION

USING GAMMA RADIATION PROFILING

by

Christopher L. Schrage

A THESIS

Presented to the Faculty of

The Graduate College at the University of Nebraska

In Partial Fulfillment of Requirements

For the Degree of Master of Science

Major: Electrical Engineering

Under the Supervision of Professor Sina Balkir and Professor Michael Hoffman

Lincoln, Nebraska

October, 2011

ISOTOPE IDENTIFICATION AND SOURCE DIRECTIONAL DETERMINATION

USING GAMMA RADIATION PROFILING

Christopher L. Schrage, M.S.

University of Nebraska, 2011

Advisers: Sina Balkir and Michael Hoffman

Gamma radiation detection is an important aspect in several industries today. These industries range from commercial, such as medical, mining, and foundry, to areas in the field of nuclear research and national security. In each industry there is a constant focus to ensure the safety of its workers and the protection of those who could be harmed. Therefore, there is a continued need to develop a system that can provide immediate and accurate knowledge of when, where, and how much gamma radiation may be present at any given time.

This thesis presents a method for evaluating gamma radiation profiles using a low power gamma radiation detector system (GRDS). This method enables multiple radioactive gamma isotopes to be identified and determine the respective vector directions of those sources relative to the GRDS location. This detection method must be accurate, implemented as a handheld or fixed solution, and have a suitable battery life for a variety of industrial needs.

This paper will first explain the low power GRDS that was used for developing these detection methods. The target gamma isotopes that are used for validating these methods will be described along with explaining the different particle interactions that occur within the system. A set of mathematical models are developed to describe the

theoretical outputs of the GRDS profiles given various gamma source configurations. These theoretical models are then used as a foundation to create algorithms for gamma isotope identification and source directional detection.

The algorithm architecture and the code level details to implement these functions will be explained. The algorithms are developed and validated using an independent software tool and simulated with a set of gamma source configurations before porting the functions to be run on the GRDS. The thesis will conclude by showing the results obtained by running the GRDS algorithms against a set of gamma source configurations to determine the accuracy of the system, and examine how the results map to the theoretical models.

Table of Contents

List of Tables

List of Figures

List of Equations

List of Code Functions

Acknowledgements

Foremost, I would like to express my sincere gratitude to my advisers Dr. Sina Balkir and Dr. Michael Hoffman for providing me an opportunity to complete my thesis work remotely in Folsom, California. Their guidance and support helped me during all the time of my research and writing of this thesis through their direction, enthusiasm, and immense knowledge.

I would like to thank Dr. Khalid Sayood for being a part of my examining committee and for his insightful comments, questions, and feedback. My sincere thanks also go to Dr. Nathan Schemm for his personal instruction and enabling me to acquire the hardware and materials needed to complete my thesis research.

I would like to thank Intel Corporation and my supervisor Hope Merritt, III. for the support, flexibility, and time to finish the coursework for my degree.

Finally, I would especially like to thank my wife Josilyn and my family for their constant encouragement, patience, and support.

Chapter 1: Introduction

Gamma radiation is produced by the decay of high energy states which occur in the atomic nucleus. When a gamma particle is released, it is emitted as a photon at a fixed wavelength and frequency. The frequencies are extremely high and typically have values above 10 exahertz (10^{19}Hz). The energies of these gamma rays tend to range from a couple hundred kilo electron volts (keV) to less than 10 mega electron volts (MeV). Gamma radiation is a form of ionizing radiation which can detach electrons from atoms or molecules and therefore considered as a health hazard for living tissue.

Since gamma radiation is a form of ionization radiation, scintillators can be used to detect and measure these gamma rays. A scintillator sensor consists of both a crystal and a photomultiplier tube (PMT). The crystal is made up of a material that exhibits luminescence by absorbing the energy of an incoming gamma particle and reemits the absorbed energy as a photon or light. Since it is difficult to electrically quantify light, the scintillator is coupled with a PMT. This PMT absorbs the emitted light and then reemits the photons in the form of electrons via the photoelectric effect. In addition to this conversion, the PMT amplifies these low charge individual electrons to an analog level which can be converted to a digital signal by an analog to digital converter (ADC). This digital data, or stream of gamma events or counts, is then input into a microcontroller to be measured, collected, processed, and analyzed.

The number of counts is proportional to the flux of incoming gamma particles onto the scintillator. This flux is dependent on both the source strength and the distance the source is from the scintillator. A detection session begins when a detector system begins to capture data. A detection session ends when the detector system stops

capturing data and begins to process the results. The total number of counts for a particular detection session is based on the particle flux and the detection session time. These factors determine the minimum number of counts required to achieve reliable results.

The gamma radiation detector system (GRDS) that was chosen to evaluate a set of methods for identifying gamma sources and determining their respective direction was developed using three scintillator sensors. This sensor array interfaces with a low power data acquisition and processing system, and evaluates the gamma radiation energies within an environment. The gamma radiation profiles generated by each sensor are jointly evaluated using a predefined set of algorithms. The output of these algorithms provided an accurate description of the gamma source configuration for any given time.

Chapter 2: Gamma Radiation Detector System (GRDS)

2.1. System Configuration

The gamma radiation detector system consists of two primary subsystems. Each of these subsystems is integrated on an independent perforated circuit board (PCB). The first PCB is the detector subsystem which integrates the three scintillator sensors, and the second PCB is the computation subsystem which integrates the ADC, processor, memory, logic, and USB interface. An image of the GRDS assembly and independent subsystems are illustrated in **Figure 2.1**.
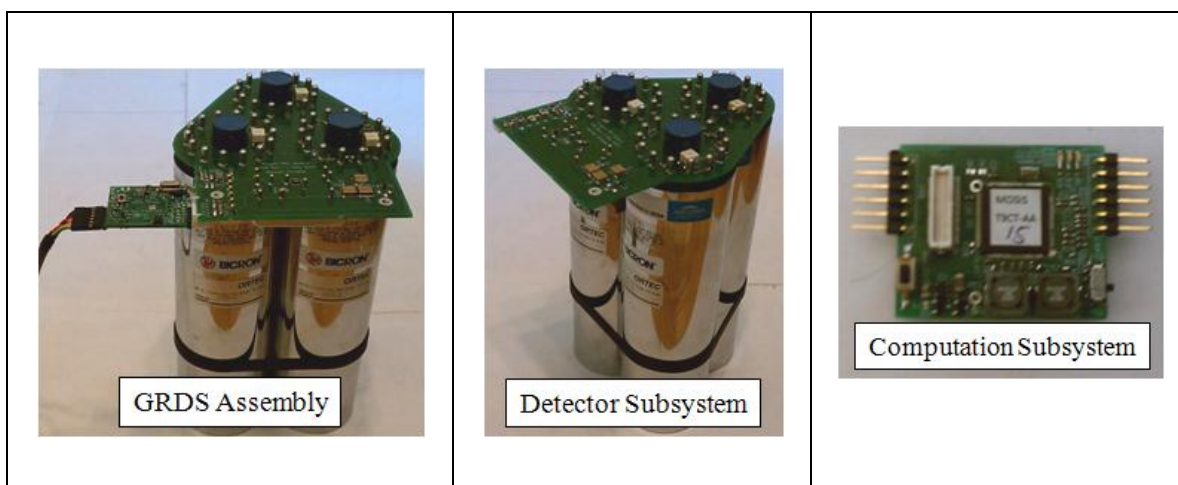
Figure 2.1: Gamma Radiation Detector System

2.1.1. Detector Subsystem

The detector subsystem consists of three Ortec 905-3 scintillator sensors [1] arranged within a radial configuration with each sensor separated by 60 degrees. The scintillator crystal is a thallium-activated sodium iodide (NaI) material and is coupled by a photocathode to an integrated PMT. The photocathode is what converts the emitted photons to photoelectrons and amplifies them through a series of dynode stages within the PMT. The amplified photoelectrons are then collected at the anode of the PMT which

is connected to a corresponding charge sensed amplifier and ADC on the computation subsystem PCB.

Each of the scintillator crystals and the PMT has a radius of 2.0". The crystal has a height of 2.0" and each sensor is encased in a metal assembly with a radius of 2.2" and soldered to the detector subsystem PCB. The coordinate system of the sensor array is described in **Table 2.1**.

Table 2.1: Scintillator Crystal Midpoint Coordinates for the Sensor Array

Sensor	X Value	Y Value	Z Value	Longitude Angle
D1	$x_1 = 0.67"$	$y_1 = 1.16"$	$z_1 = 1.0"$	$\theta = 60°$
D2	$x_2 = -1.33"$	$y_2 = 0.0"$	$z_2 = 1.0"$	$\theta = 180°$
D3	$x_3 = 0.67"$	$y_3 = -1.16"$	$z_3 = 1.0"$	$\theta = 300°$

Each coordinate value in **Table 2.1** represents the midpoint of each scintillator crystal. These values will be used to model the GRDS outputs with various gamma source configurations.

2.1.2. Computation Subsystem

The computation subsystem implements a custom low power Texas Instruments MSP430 microcontroller chip (NSP430) [2]. The computation subsystem consists of an 8 bit ADC for each of the three sensors, I/O hardware, timers, and 48kB SRAM of memory. The chip was designed and fabricated using a 0.18μm CMOS technology process and has package dimensions of 3mm x 3mm. The ADC is powered by an event driven clocking mechanism independent from the processor clock and only samples when a gamma event is detected. The chip implements a strict power management scheme which enables the processor to sleep until at least 12 gamma events are detected by the

sensors. If the processor is woken up, it processes the counts that are in each of the sensor FIFO buffers and determines if a detection session is needed before going back to sleep. Another implementation option for this system could be to periodically measure the environment at a set time interval.

In memory, each sensor maintains 256 individual counters or buckets to track the gamma events for a target energy range. Each bucket represents a granular energy value which corresponds to the analog voltage measured by the ADC. Every gamma event detected by each sensor is measured and compared against each of the bucket energy values. If the bucket falls within that measured energy range, then its respective counter is incremented. After a detection session is complete, these bucket counters are read to create a histogram for each sensor and then evaluated. **Figure 2.2** illustrates a basic block diagram of the detector and computation subsystems.
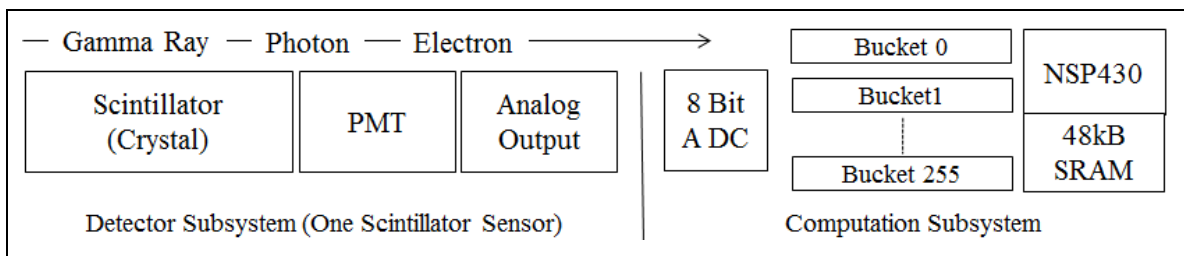
Figure 2.2: GRDS Subsystem Block Diagram

2.2.   Gamma Sources

A gamma source emits gamma radiation and is based on a variant of a particular atomic element called an isotope. Isotopes have different numbers of neutrons compared to atoms of a particular element which have the same number of protons. For these particular atoms this creates an instability which is observed by certain isotopes emitting ionizing particles or gamma rays through radioactive decay.

Four gamma sources were chosen to quantify both the mathematical models and develop the algorithms to be run on the computation subsystem. These sources were procured from Spectrum Technologies located in Oak Ridge, Tennessee, USA, and were part of the Model RSS 8 Gamma Source set. Each source has a radioactive value of one micro curie (uCi) and is considered as a quantity exempt to regulation by the United States Nuclear Regulatory Commission.

The specific isotopes selected are Barium[133], Cesium[137], Manganese[54], and Cobalt[60]. Their respective radioactive attributes are described in **Table 2.2**.

Table 2.2: Selected Gamma Source and Respective Attributes

Isotope	Barium[133]	Cesium[137]	Manganese[54]	Cobalt[60]
Sample				
Energy	356 keV	661 keV	834 keV	1173 keV
Half Life	10.5 Years	30.07 Years	312.3 days	5.27 Years

Each source sample is 1.0" in diameter with the actual radioactive element equal to 0.25" in diameter. **Figure 2.3** illustrates a picture and a diagram of the reverse side of an individual gamma source.
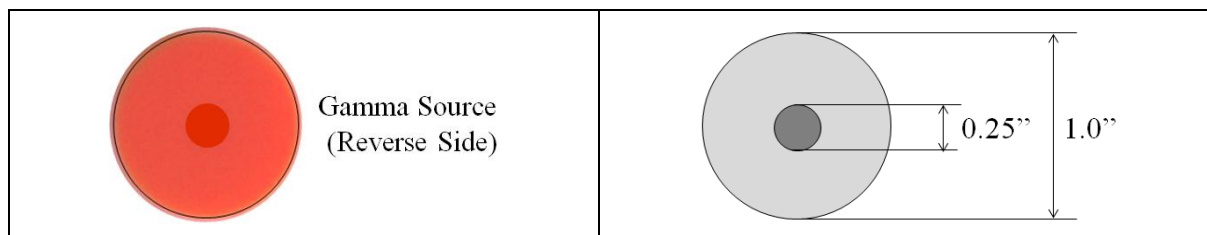
Figure 2.3: Gamma Source Dimensions

2.3.   Gamma Ray Interactions

During a gamma event, there are three interactions that can occur when an incident gamma ray from a gamma source bombards with atomic electrons in the scintillator crystal. These interactions need to be mitigated because there can be impact to both the photoelectric energy that exits the PMT and the respective energy that is measured by the GRDS. It is also possible that there will be no interaction. The three interactions that can occur for an incident gamma ray are defined as either photoelectric absorption, Compton scattering, or pair production. These energy impacts will result in either an equal or a lower photoelectric energy than the incident gamma ray energy [3].

2.3.1. Photoelectric Absorption

Photoelectric absorption is a particle effect that occurs when a gamma ray bombards with an atomic electron and the gamma energy, minus the binding electron energy, is transferred to that electron. This interaction creates both a photoelectron and an emitted x-ray that is equal to the electron binding energy.   The photoelectron and the x-ray are both absorbed by the scintillator crystal and a light pulse is created which is proportional to the incident gamma ray energy. This interaction is illustrated in **Figure 2.4**.
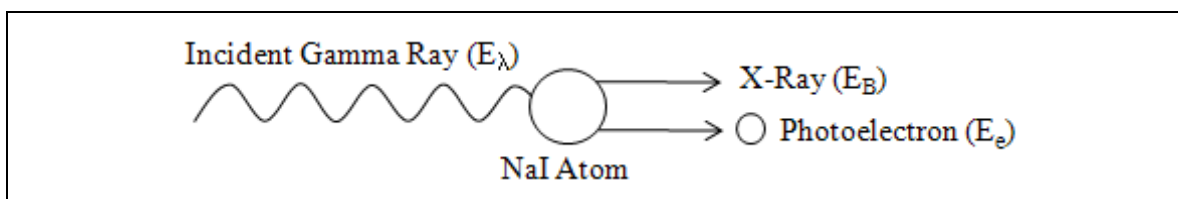
Figure 2.4: Photoelectric Absorption Effect

Photoelectric absorption is the preferred interaction because it causes the resulting photoelectric energy from the PMT to fall within the same energy range as the incident gamma ray.

2.3.2. Pair Production

Pair production is a particle effect that occurs when an incident gamma ray is in the vicinity of an atomic nucleus and creates an electron-positron pair. For this interaction to occur, the gamma ray energy must be at least 1.022 MeV because this is the energy required to create the electron-positron pair. During the generation of this pair, at least 0.511 MeV is transferred to each particle, and any remaining energy is shared between the electron and the positron as kinetic energy. This interaction is illustrated in **Figure 2.5**.
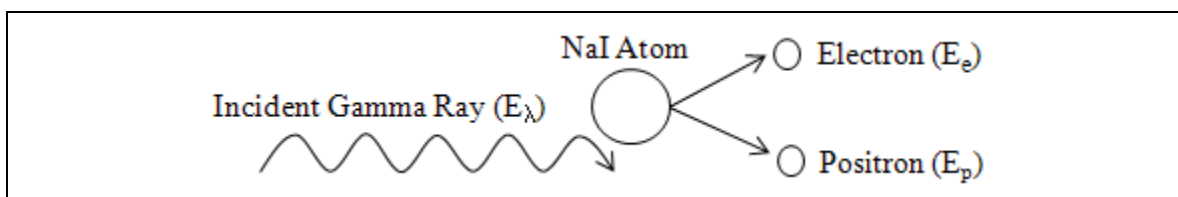
Figure 2.5: Pair Production Effect

Any kinetic energy lost by the electron and positron pair is absorbed by the scintillator crystal. However, after the electron and positron lose its kinetic energy, the particles may recombine to create two gamma rays, each with energy of 0.511 MeV. The photoelectric energy from the PMT will then be dependent on these gamma rays escaping or getting absorbed by the scintillator crystal. If both escape, then the photoelectric energy from the PMT will be equal to the kinetic energy. If one escapes then the photoelectric energy will be equal to the kinetic energy plus 0.511MeV. If neither of the

gamma rays escapes then the photoelectric energy will be equal to the kinetic energy plus

1.022 MeV, which should equal the original energy of the incident gamma ray.

Pair production is an interaction of concern for gamma ray energies greater than

1.022 MeV because this can sometimes result in multiple photoelectric energies from the

PMT that are lower than the incident gamma ray. However, if neither of the gamma rays

escapes, pair production is of minimal concern as the photoelectric energy will be equal

to the incident gamma ray.

2.3.3. Compton Scattering

Compton scattering is a particle effect that occurs when a gamma ray interacts

with a free or weakly bound electron and transfers part of its energy to that electron. The

energy transferred to the electron is in the form of kinetic energy, and since the electron

binding energy is very small, the amount of kinetic energy is almost equal to the energy

lost by the gamma ray. The angle at which the gamma ray intercepts the electron

determines the amount of energy that is transferred. This interaction is illustrated in

Figure 2.6.
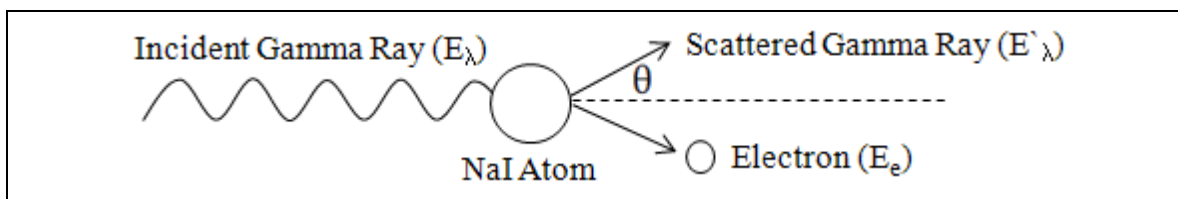
Figure 2.6: Compton Scattering Effect

Compton scattering is an interaction of concern because this can sometimes result

in photoelectric energies from the PMT that are lower than the incident gamma ray. This

energy would be equal to the kinetic energy of the electron, or the energy lost by this

interaction from the incident gamma ray.   However, if the scattered gamma ray is fully

absorbed by the scintillator crystal and is combined with the kinetic energy lost from the

free electron, Compton scattering becomes of minimal concern as the photoelectric

energy will be equal to the incident gamma ray.

Chapter 3: Sensor System Mathematical Modeling

Determining the isotope type and direction are the two primary GRDS functions when evaluating the gamma radiation profile for a given detection session. Isotope identification can be assessed by evaluating histogram peaks in the target energy ranges. Additionally mathematical models can be developed to describe theoretical expectations on how direction could be evaluated. These models describe the energy profiles for each scintillator sensor as a source rotates around the sensor array, while taking into account both source distance and the exposed sensor surface area to the source. These models are initially evaluated as three independent models, as described below, but later combined to create a comprehensive directional model.

1. **Longitude Movement Model:** This model describes the varying distance from the midpoint of each sensor's scintillator crystal as a source rotates around the detector subsystem. This rotation path occurs in what will be referred to as the x-y plane, or $0 \leq \theta < 360°$.

2. **Latitude Movement Model:** This model describes the varying distance from the midpoint of each sensor's scintillator crystal as a source rotates around the detector subsystem. This rotation path occurs in what will be referred to as the y-z plane, or $0 \leq \phi < 360°$.

3. **Sensor Shadowing Model:** This model describes the proportional surface area of each sensor's scintillator crystal that is not exposed or shielded as a source rotates around the detector subsystem. This rotation path occurs in what will be referred to as the x-y plane, or $0 \leq \theta < 360°$.

These three mathematical models are determined based on the dimensions of each individual sensor, the coordinates of the scintillator crystal midpoint, and the orientation of the sensor array. These are illustrated in **Figure 3.1**.
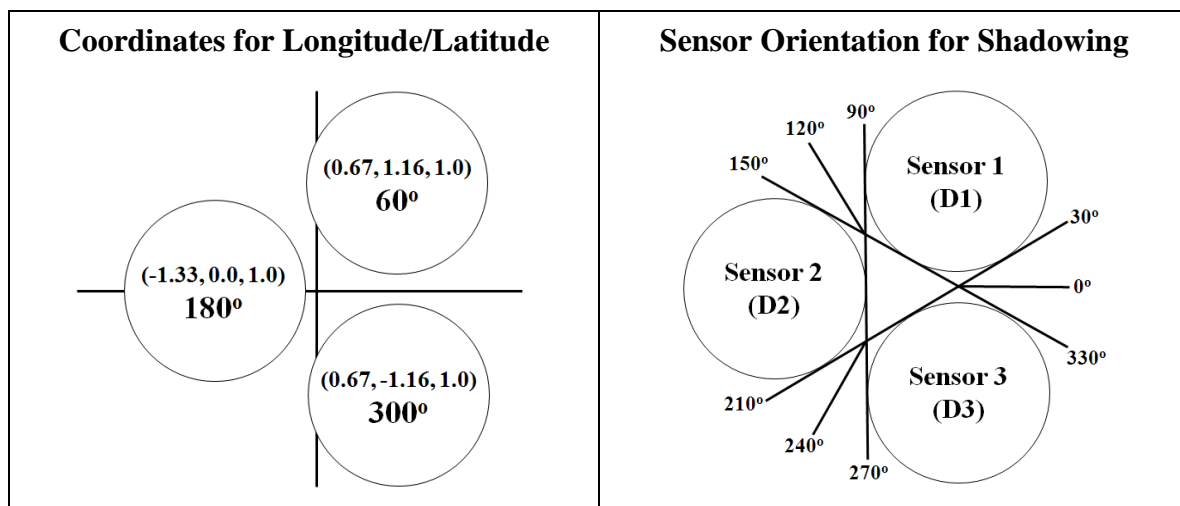
Figure 3.1: Sensor Array Coordinates and Orientation for Mathematical Modeling

The angles illustrated in **Figure 3.1** with respect to the sensor orientation are not necessarily the same radial angles used to describe a source rotating around the sensor array. These angles are created by the intersection of the sensor boundaries and are required for evaluating the sensor shadow model. The sensor boundary intersection angles will only tend to equal the source angles at far field source distances which will be discussed during the evaluation of the shadow model.

3.1. Longitude Movement Model

It is expected that the number of gamma events is proportional to the distance the source is from each sensor. This proportionality means that as the source distance increases, the number of counts decreases. Therefore, evaluating the varying distance as a source rotates around the sensor array provides a relative expectation of the count

values recorded by each sensor. As a result, these counts would fall within the same

energy range as the gamma source.

A source that rotates around the sensor array in the x-y plane and maintains a

fixed circular radial distance will create an oscillating distance d1 from sensor D1, an

oscillating distance d2 from sensor D2, and an oscillating distance d3 from sensor D3.

To illustrate this oscillating distance the linear distance equation is applied to the (x, y)

coordinates of each sensor's crystal midpoint, along with the (x, y) coordinates of the

source as it rotates around the sensor array from $0 \leq \theta < 360°$. These linear equations

for d1, d2, and d3 are expressed in **Equation 3.1**, where r is the fixed radial source

distance and θ is the source angle from the middle of the detector subsystem.

$d_1(\theta) = \sqrt{(r \cdot \cos\theta - x_1)^2 + (r \cdot \sin\theta - y_1)^2}$	$x_1 = 0.67"$	$y_1 = 1.16"$
$d_2(\theta) = \sqrt{(r \cdot \cos\theta - x_2)^2 + (r \cdot \sin\theta - y_2)^2}$	$x_2 = -1.33"$	$y_2 = 0.0"$
$d_3(\theta) = \sqrt{(r \cdot \cos\theta - x_3)^2 + (r \cdot \sin\theta - y_3)^2}$	$x_3 = 0.67"$	$y_3 = -1.16"$

Equation 3.1: Longitude Movement for a Revolving Source about a Sensor Array

The equations in **Equation 3.1** provide a source distance from each sensor

relative to the other sensors in the array. Each distance then represents a proportional

value to the expected flux of gamma events, or activity ratio (a_i), expected at each sensor

for a given longitude angle. This activity ratio needs to also incorporate the fact that a

closer source distance creates a higher activity and a further source distance creates a

lower activity. Therefore, the activity ratio for each sensor is calculated by comparing

and normalizing its activity value to the total activity of all sensors in the array. Then, to

express the inverse relationship between source distance and sensor activity the result is

subtracted from a maximum normalized value. This is described in **Equation 3.2**.

$$a_i(\theta) = 1000 - \left[\left(\frac{d_i(\theta)}{d_1(\theta) + d_2(\theta) + d_3(\theta)}\right) \cdot 1000\right] \qquad i = 1, 2, 3$$

Equation 3.2: Sensor Activity Ratio for Longitude Movement

To put less emphasis on decimal points, and provide a reasonable integer value output, **Equation 3.2** uses 1000 as the maximum normalized value. In addition, the NSP430 will need to process this equation and there are no floating point processing units available. Therefore, all functions and results will be processed as integer calculations and any fractional values will be discarded.

By applying both **Equation 3.1** and **Equation 3.2** for all sensors in the array and for gamma source longitude angles $0 \leq \theta < 360°$, the following activity plot, or longitude directional model, is generated and illustrated in **Figure 3.2**.
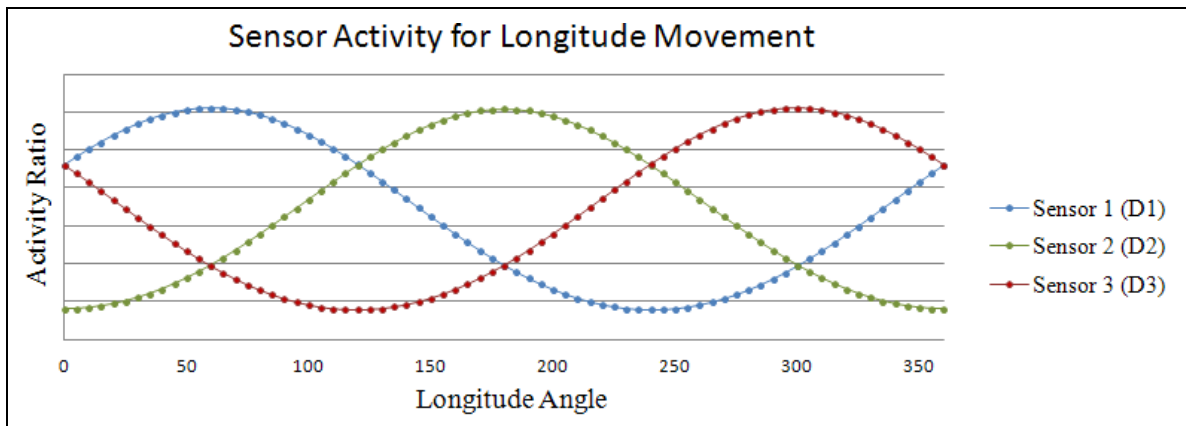
Figure 3.2: Sensor Activity Model for Longitude Directional Movement

Figure 3.2 illustrates that the activity ratio value for each sensor is distinct and varies at each sensor when a source rotates along a fixed longitude path. This figure also illustrates that due to the symmetry of the sensor array, there is a repeating pattern that exists every 60 degrees from $0 \leq \theta < 360°$. These same equations for the longitude directional model can also be used to determine how the activity curves will be affected when the source distance changes. By plugging in varying values for the source distance

(r), there exists a proportional relationship between the amplitude of the activity curves and the source distance. The activity curve amplitude is defined by the minimum trough and maximum crest values for a given longitude directional model. These values are apparent by evaluating the activity ratio curves for all three sensors for any given 180° range.

The source distance can be characterized as either being in a near field or far field zone. The near field will produce curves with much larger amplitudes and therefore easier to quantify distinct activity ratio values at each longitude angle. However, as the distance increases the amplitude of each activity curve decreases and therefore the activity ratio values become less distinct between each sensor. Longitude directional models that have smaller amplitudes will also have smaller margins for accuracy. These margins will be subject to errors in the system, and can be further impacted by scintillator crystal efficiencies, gamma ray interactions, and thresholds in the detection algorithms. **Table 3.1** compares the activity curve amplitudes and respective sensitivity threshold as the source distance is increased from 3.0" (near field) to 1000.0" (far field).

Table 3.1: Activity Curve Amplitudes as a Function of Source Distance

Zone	Distance	Max Value	Min Value	Amplitude	Sensitivity Threshold
Near Field	3.0"	822	545	277	1.54
	10.0"	712	623	88	.49
	200.0"	669	664	5	.02
Far Field	1000.0"	667	666	1	.01

The sensitivity threshold in **Table 3.1** describes the activity ratio value per degree and is used as a metric for determining the allowable error for the directional model.

This is calculated by dividing the amplitude by 180 degrees. The acceptable sensitivity threshold value and the far field effects are dependent on the sensor array configuration. Although an isotope can still be identified with a strong enough source and a long enough detection session, determining direction would still be an issue if the sensitivity threshold is too small. One way to alleviate this problem is to increase the distance between each of the sensors in the detector subsystem. This would enable a more distinct activity ratio value for each sensor at further source distances, but would have to be a design decision based on the intended usage of the GRDS.

3.2.   Latitude Movement Model

The longitude model describes how the sensor activity changes when the source rotates around the x-y plane. The latitude model describes how the sensor activity changes when the source rotates about the y-z plane. The circular angle rotation range is still the same, but the angle is now expressed as ϕ instead of θ, and the sensor crystal midpoint z-value determines where $\phi = 0°$. The same linear equation concepts still apply as in the longitude model, however the source radial distance in the x-y plane is no longer fixed. The radial source distance in the x-y plane now depends on the y-value and z-value created by each ϕ angle as shown in **Figure 3.3**.
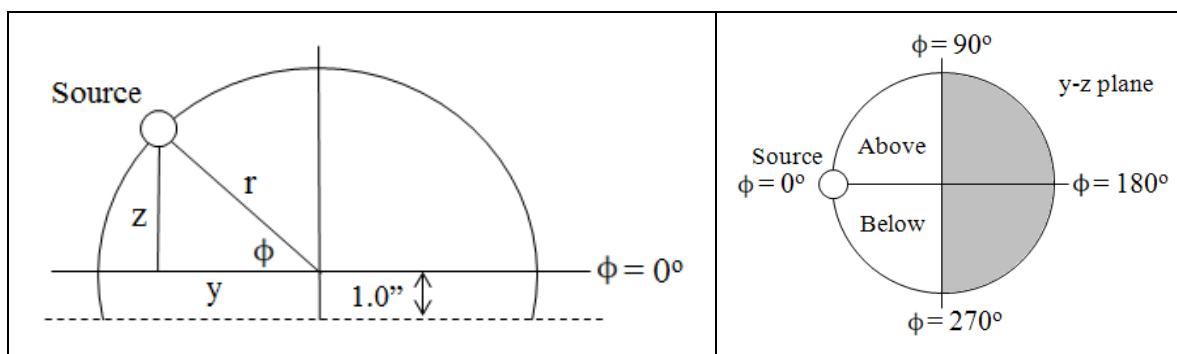
Figure 3.3: Source Distance for Latitude Directional Movement

To calculate the latitude source distance using the linear equations from the
longitude model, both the y-value and z-value illustrated in **Figure 3.3** needs to be
calculated. These values are expressed in **Equation 3.3**. The radial source distance in the
y-z plane is expressed as r and is equal to the radial distance in the x-y plane.

$y_\phi = r \cdot \cos \phi$	$z_\phi = r \cdot \sin \phi$

Equation 3.3: Latitude Movement Values for Y and Z

The y-value in **Equation 3.3** represents the new radial source distance for the
longitude model. **Equation 3.4** substitutes this y-value in for r to determine the x-y
radial source distance for a given latitude angle.

$$d_i(\phi)_{Lat} = \sqrt{(y_\phi \cdot \cos \theta - x_i)^2 + (y_\phi \cdot \sin \theta - y_i)^2}$$

Equation 3.4: Longitude Source Distance for Given Latitude Angle

In order to determine the final distance for a given longitude and latitude angle,
the value calculated in **Equation 3.4**, along with the z-value calculated in **Equation 3.3**,
is used in conjunction with the coordinates of each sensor's crystal midpoint and
Pythagoreans theorem. This is expressed in **Equation 3.5**.

$d_i(\theta, \phi) = \sqrt{d_i(\phi)_{Lat}{}^2 + (z_\phi)^2}$	$i = 1, 2, 3$

Equation 3.5: Source Distance for Longitude and Latitude Directional Movement

The same activity ratio equation that was used in the longitude movement model
is redefined in **Equation 3.6** to equate activity ratios for both longitude and latitude
angles.

$a_i(\theta, \phi) = 1000 - \left[\left(\dfrac{d_i(\theta, \phi)}{d_1(\theta, \phi) + d_2(\theta, \phi) + d_3(\theta, \phi)} \right) \times 1000 \right]$	$i = 1, 2, 3$

Equation 3.6: Sensor Activity Ratio for Longitude and Latitude Directional Movement

It is difficult to illustrate **Equation 3.6** as a single plot for all longitude and latitude angles, so **Figure 3.4** illustrates three longitude directional models, each with a source radius at 3.0" and a different fixed latitude angle.

$a_i(\theta, 0°)$ $0 \le \theta < 360°$ Amplitude $= 88$	
$a_i(\theta, 45°)$ $0 \le \theta < 360°$ Amplitude $= 62$	
$a_i(\theta, 75°)$ $0 \le \theta < 360°$ Amplitude $= 22$	
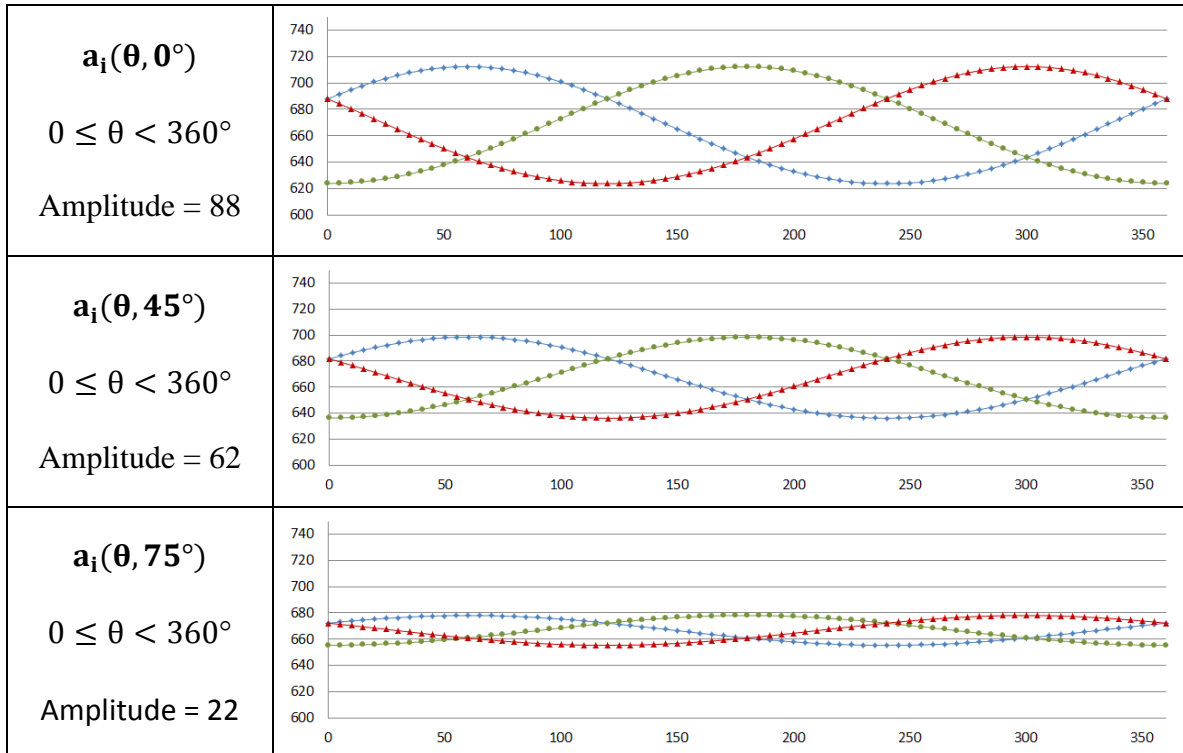
Figure 3.4: Longitude Directional Model as a Function of Latitude

The resulting longitude curves shows that there is a compression or squishing effect that occurs depending on the latitude angle. This can be characterized in more detail by identifying the latitude angle that produces the maximum amplitude for an activity curve and then comparing that amplitude to all other activity curves for all latitude angles. This squishing effect is illustrated in **Figure 3.5** for $0 \le \phi < 360°$.
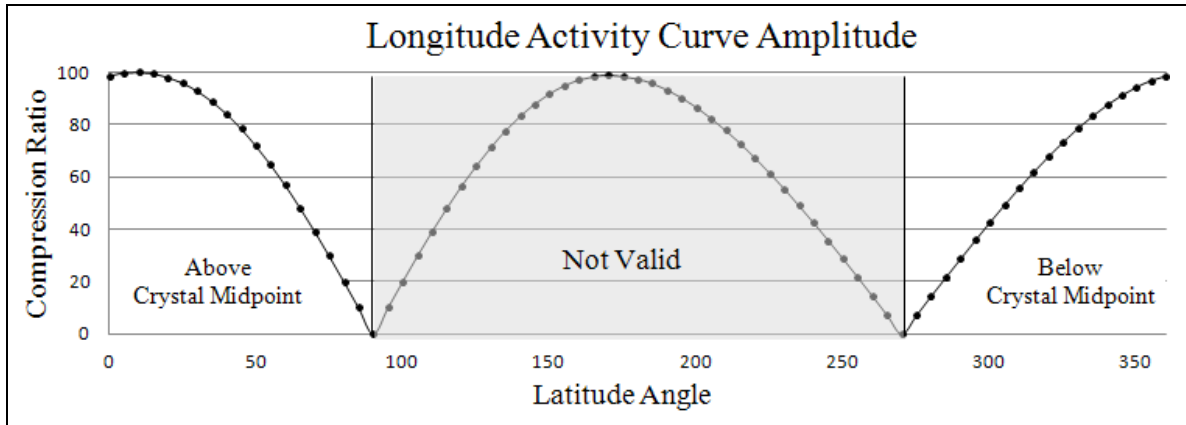
Figure 3.5: Amplitude Compression Between $0 \leq \phi < 360°$

According to **Figure 3.5** the latitude curve is only valid between $270 \leq \phi \leq 90°$, where values between $0 \leq \phi \leq 90°$ represent directional values above the scintillator crystal midpoint, and values between $270 \leq \phi \leq 0°$ represent directional values below the scintillator crystal midpoint. Latitude values between $90 < \phi < 270°$ are considered not valid because these angles represent a different longitude angle $180°$ from the source longitude angle.

At $\phi = 90°$ and $\phi = 270°$ the activity ratios between all three sensors will be equal and the amplitude will be zero. Although small amplitudes and sensitivity thresholds were described previously as a concern in the longitude only model, it is not a concern for the longitude-latitude model, because amplitude compression can be a characteristic of a specific latitude angle. However, the amplitude for $\phi = 0°$ should still be evaluated to determine if there is enough overhead available for all compression ratios. This will ensure the sensitivity thresholds between all latitude angles will provide enough distinction between each sensor's activity ratios.

3.3.   Sensor Shadowing Effect Model

The linear equations for the longitude and latitude mathematical models provide a good foundation for determining how the activity will vary as a gamma source rotates about the x-y-z axis. However, these models do not provide an understanding for how the activity ratios may vary based on the orientation of the sensors in the array. Since each of the sensors is arranged in a radial configuration there are longitude angles where an individual sensor may be partially or fully shielded by other sensors. This shielding or shadowing effect from other sensors will cause attenuation in the directional model amplitude. This shadowing will vary based on which of the following regions the gamma source is in with respect to a particular sensor.

1. **Unity Region:** This region applies to an angle range where a sensor has full exposure to the gamma source and there is no shielding exhibited from any other sensor.

2. **Attenuation Region:** This region applies to an angle range where a sensor exhibits either increased or decreased shadowing from a gamma source because of shielding by one other sensor.

3. **Tunnel Region:** This region applies to an angle range where a sensor exhibits increased or decreased shadowing from a gamma source because of shielding by two other sensors.

4. **Dark Region:** This region applies to an angle range where a sensor has no direct exposure to the gamma source and exhibits full shielding by one other sensor.

Each of these regions will be evaluated separately to determine a shadowing

coefficient (τ) that can be applied to each angle in the longitude and latitude directional

models. The shadowing coefficient will have a scaling value between $0 \le \tau \le 100\%$

and depend on both the gamma source direction and the position of each individual

sensor.

As described previously, all sources are assumed to radiate outward and

uniformly, and will create what is called an incident vector with each sensor. This vector

defines a sensor boundary at which the shadowing ends and exposure to the source

begins. In addition, this vector exhibits both near field and far field limits based on the

gamma source distance from the sensor array. An example of incident vectors and the

shadowing differences between near field and far field source directions are illustrated in
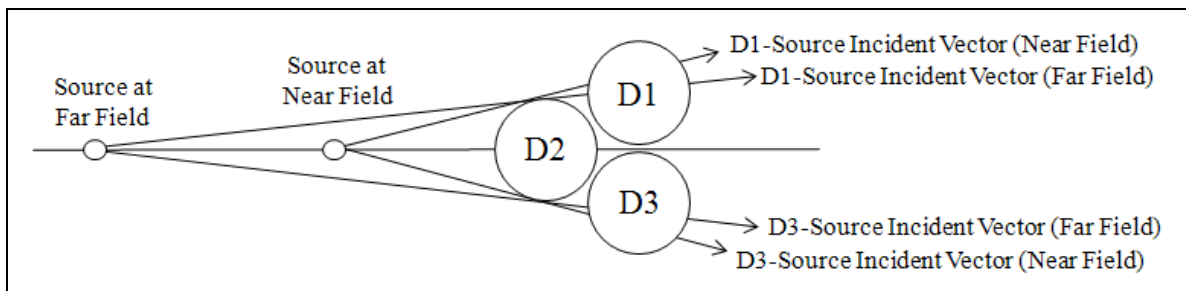
Figure 3.6.

Figure 3.6: Shadowing Differences with a Source at Near Field and Far Field

In the configurations illustrated in **Figure 3.6**, the gamma source is placed

at $\theta = 180°$. There is a shadowing of sensor D1 by D2 and a shadowing of sensor D3 by

D2. Based on the sensor intersection of these incident vectors the shadowing effects

exhibited by D1 and D3 are greater in the near field compared to the gamma source in the

far field.

3.3.1. Unity Region Shadowing

When the gamma source is in this angle region for a particular sensor, there is no shadowing effect by another sensor that would alter the longitude or latitude curves. Therefore, the shadowing coefficient for this region is $\tau = 0\%$. Based on the coordinates and sensor array orientation described in **Figure 3.1**, a set of linear equations can be developed to calculate the source angles that would fall within the unity region. **Table 3.2** lists each of the sensor's boundary angles and the reference points used to generate each equation. It is important to note that the Point 1 coordinates are not at the origin of the sensor array, but at the point where the boundary angles intersect.

Table 3.2: Linear Equations for each Boundary Angle in the Unity Region

Sensor	Angle	Point 1	Point 2	Linear Equation
D1	150°	(-0.33, 0.58)	$P1 + (\cos 150°, \sin 150°)$	$y = -0.58x + 0.39$
D1	330°	(0.67, 0.0)	$P1 + (\cos 330°, \sin 330°)$	$y = -0.58x + 0.39$
D2	90°	(-0.33, 0.58)	$P1 + (-0.33, 0.0)$	$x = -0.33$
D2	270°	(-0.33, -0.58)	$P1 + (-0.33, 0.0)$	$x = -0.33$
D3	30°	(0.67, 0.0)	$P1 + (\cos 30°, \sin 30°)$	$y = 0.58x - 0.39$
D3	210°	(-0.33, -0.58)	$P1 + (\cos 210°, \sin 210°)$	$y = 0.58x - 0.39$

It is expected that the boundary angles described in **Table 3.2** are only valid as source angles for the extreme far field case or source distances equal to infinity. In order to calculate the near field case or what is considered as source distance equal to 3.0", each linear equation needs to be evaluated using the source path equation defined by **Equation 3.7**.

Source Path $\rightarrow x^2 + y^2 = r^2$	$r =$ Source Path Radius

Equation 3.7: Source Path Equation for Longitude Movement

By defining a source path radius of 3.0" and then setting each of the linear equations in **Table 3.2** equal to **Equation 3.7** the unity region can be evaluated by determining where these lines intersect. The resulting angle is then calculated by evaluating this point with respect to the sensor array origin. The same can be done for a source path radius of infinity. The results of both source distances are expressed in **Table 3.3**.

Table 3.3: Sensor Angle Ranges for Unity Region Shadowing

Sensor	Zone	Distance	Angle Range	Coefficient
D1	Near Field	$r = 3.0"$	$336.5 \leq \theta \leq 143.5°$	$\tau = 0\%$
	Far Field	$r = \infty$	$330.0 \leq \theta \leq 150.0°$	$\tau = 0\%$
D2	Near Field	$r = 3.0"$	$96.5 \leq \theta \leq 263.5°$	$\tau = 0\%$
	Far Field	$r = \infty$	$90.0 \leq \theta \leq 270.0°$	$\tau = 0\%$
D3	Near Field	$r = 3.0"$	$216.5 \leq \theta \leq 23.5°$	$\tau = 0\%$
	Far Field	$r = \infty$	$210.0 \leq \theta \leq 30.0°$	$\tau = 0\%$

Table 3.3 describes the unity region for this GRDS and shows that as the source distance increases, the unity region increases to a far field limit for each sensor. In these regions no attenuation due to shadowing will be observed at these source angles.

3.3.2. Attenuation Region Shadowing

The shadowing coefficient for the attenuation region can vary between $0 < \tau < 100\%$ when shielding occurs from only one sensor. To evaluate which particular coefficient should be applied for each angle, the point at which the incident vector enters the sensor and exits the sensor needs to be determined. These two points create a line segment with the target sensor, and this line segment is used to evaluate the partially exposed area of the sensor. This area is then compared with the total area of the sensor to

determine how much of the sensor is shielded. This resulting percentage is what is

assigned as the shadowing coefficient for that source angle.

In order to evaluate the incident vector area, the segment angle of the line

segment with respect to the sensor origin needs to be calculated. This can be evaluated

by first defining two right triangles with respect to the sensor's $y = 0$ origin line and the

line segment. This is illustrated in **Figure 3.7**.
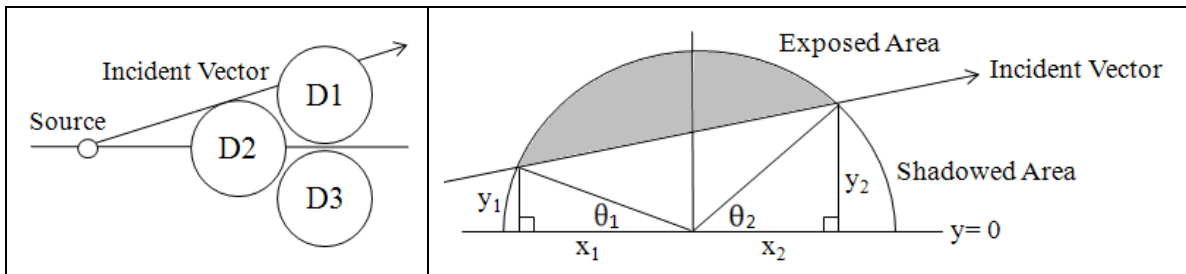
Figure 3.7: Incident Vector for Sensor D1 with Source @ $\theta = 180°$

The θ_1 and θ_2 angles created by the two right triangles are used to calculate the

incident vector segment angle.   Once the segment angle is calculated this value is used in

conjunction with the sensor radius to equate the exposed sensor area. The segment area

is the shaded area in **Figure 3.7**, and the equations for calculating segment area are

described in **Equation 3.8** and **Equation 3.9**.

$\theta_1 = \tan^{-1}\left(\frac{y_1}{x_1}\right)$	$\theta_2 = \tan^{-1}\left(\frac{y_2}{x_2}\right)$	$\theta_{Segment} = 180° - \theta_1 - \theta_2$

Equation 3.8: Segment Angle from Incident Vector

$\text{Segment Area} = \frac{r^2}{2} \cdot \left[\left(\frac{\pi}{180}\right) \cdot \theta_{Segment} - \sin\theta_{Segment}\right]$	$r = 1.0''$

Equation 3.9: Exposed Sensor Area from Incident Vector

Once the segment area is calculated, this can be compared to the total x-y area of

the sensor crystal to determine the shadowed sensor area. This comparison is described

in **Equation 3.10** and results to a percentage which defines the shadowing coefficient for a particular incident vector and source angle.

$$\text{Shadowing Coefficient } (\theta_{Source}) = \frac{\text{Segment Area}}{\pi r^2}$$

Equation 3.10: Shadowing Coefficient for Incident Vector

The primary challenge with determining the segment area is equating the x and y values for each right triangle. Therefore, instead of evaluating each value independently, a standard plot can be developed to show the relationship between shadowing coefficients and segment angles. **Figure 3.8** illustrates this plot with respect to **Equation 3.9** and **Equation 3.10** for $0 \leq \theta_{Segment} < 360°$.
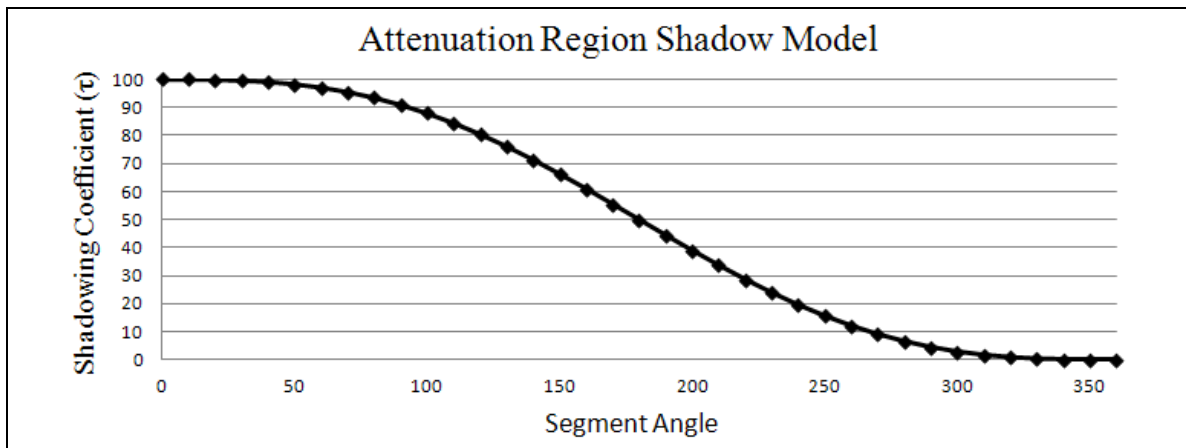
Figure 3.8: Shadowing Coefficient as a Function of Segment Angle

The curve illustrated in **Figure 3.8** provides a base model for evaluating the shadowing effects for a particular sensor when the source is in the attenuation region. There are two source paths in the attenuation region that will change the shadowing effects for a particular sensor. If the segment angle increases as the source moves, then the source path exhibits decreasing shadowing, but if the segment angle decreases, then the source path exhibits increasing shadowing.

In order to evaluate the source angles for the attenuation region, the angles where

the shadowing coefficient begins to decrease from $\tau = 100\%$, and where $\tau = 0\%$ need to

be determined. Shadowing boundaries where $\tau = 0\%$ was determined after evaluating

the unity region, but to calculate when $\tau = 100\%$ begins, two linear equations are

required. These equations are illustrated in **Figure 3.9**.
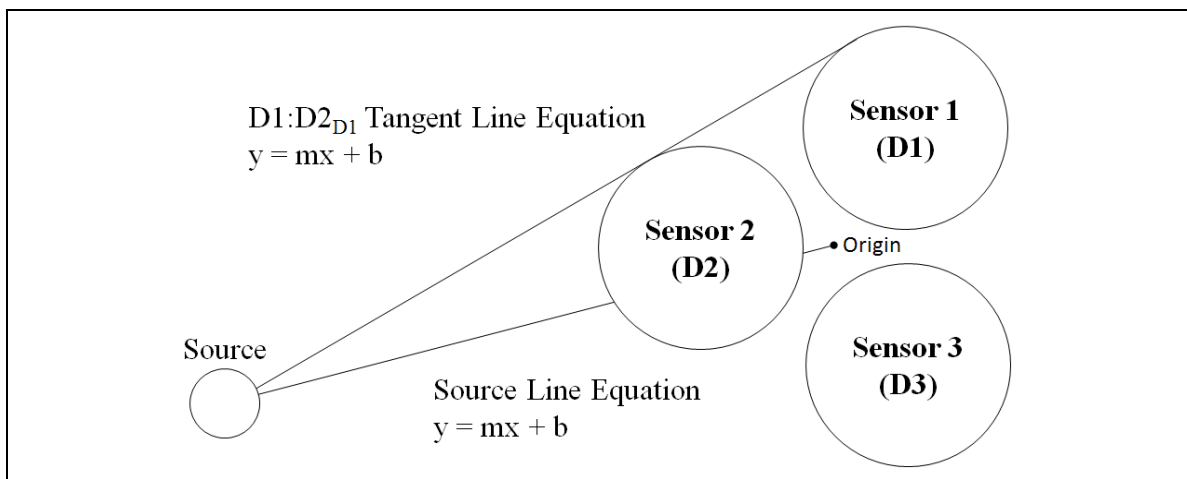
Figure 3.9: Linear Equations for Evaluating Maximum Shadowing

In the example in **Figure 3.9**, the target sensor is D1, the sensor causing the

shadowing is D2, and the tangential line is defined as D1:D2$_{D1}$. The first equation

defines the tangential line from the target sensor boundary and the sensor that is

causing $\tau = 100\%$. Using the sensor dimensions and the coordinates of the sensor array

configuration described in **Figure 3.1**, **Table 3.4** describes the tangential line equation

for each sensor and source path trajectory.

Table 3.4: Tangent Line Equations for Shadowing

Tangent Line	Target Sensor	Source Trajectory	Final Equation
D1: D2 $\theta_{Tan} = 30°, 210°$	D1 = D1:D2$_{D1}$	Clockwise	$y = 0.58x + 1.92$
	D2 = D1:D2$_{D2}$	Counterclockwise	
D1: D3 $\theta_{Tan} = 90°, 270°$	D1 = D1:D3$_{D1}$	Counterclockwise	$x = 1.67$
	D3 = D1:D3$_{D3}$	Clockwise	
D2: D3 $\theta_{Tan} = 150°, 330°$	D2 = D2:D3$_{D2}$	Clockwise	$y = -0.58x - 1.92$
	D3 = D2:D3$_{D3}$	Counterclockwise	

The second equation defines an incident vector from the source direction to the sensor array origin. This is straightforward to evaluate by using the source angle. This is described in **Equation 3.11**.

Point 1	Point 2	Equation
$P1 = (0,0)$	$P2 = (\cos \theta_{Source}, \sin \theta_{Source})$	$y = \left(\dfrac{\sin \theta_{Source}}{\cos \theta_{Source}} \right) \cdot x$

Equation 3.11: Source Direction Incident Vector with Respect to Sensor Array Origin

By setting each of the equations in **Table 3.4** equal to the source equation in **Equation 3.11**, the x-y intersect point can be evaluated for each sensor's tangent line. The distance equation can then be applied between this intersect point and the sensor array origin to determine the minimum gamma source distance for where the shadowing coefficient equal to 100% begins. To illustrate an example, **Figure 3.10** plots the minimum source distance as a function of source angle to determine at what source distance a D1:D2$_{D1}$ tangent line intersects.
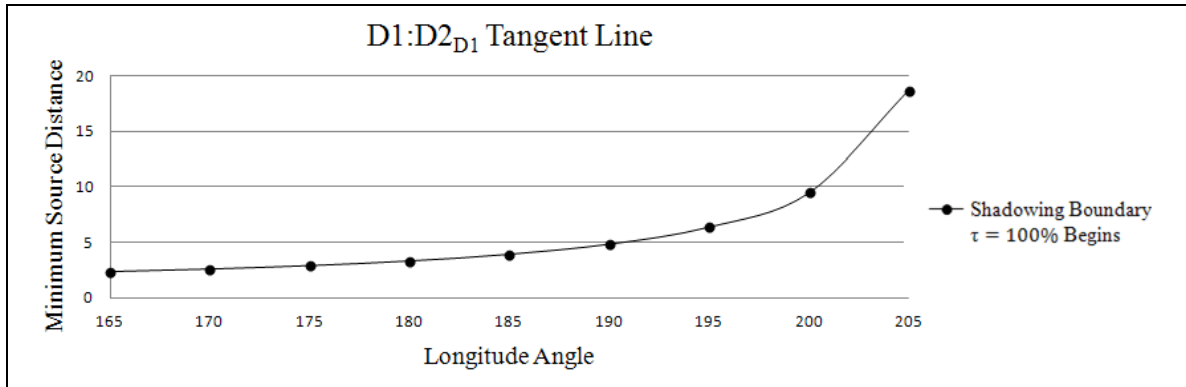
Figure 3.10: Maximum Shadowing and Minimum Source Distance for a Tangent Line

Figure 3.10 illustrates that the angle range for the attenuation region will vary

based on the source distance. **Table 3.5** shows the full range of the attenuation region

based on a source distance in the near field and in the extreme far field. These values

represent the longitude angle range for a given source distance whether the sensor is

exhibiting increasing or decreasing shadowing. Based on the attenuation shadow type,

the shadowing coefficient will either start at $\tau = 0\%$ or $\tau = 100\%$, then follow the curve

in **Figure 3.8** until reaching either the unity region or the region which $\tau = 100\%$.

Table 3.5: Sensor Angle Ranges for Attenuation Region Shadowing

Target Sensor	Angle Range Near Field, r = 3.0"	Angle Range Far Field, r = ∞	Coefficient
D1:D2$_{D1}$	$143.5 \le \theta \le 177.0°$	$150.0 \le \theta \le 210.0°$	$\tau = 0 \to 100\%$
D2:D3$_{D2}$	$263.5 \le \theta \le 297.0°$	$270.0 \le \theta \le 330.0°$	$\tau = 0 \to 100\%$
D1:D3$_{D3}$	$23.5 \le \theta \le 57.0°$	$30.0 \le \theta \le 90.0°$	$\tau = 0 \to 100\%$
D1:D3$_{D1}$	$303.0 \le \theta \le 336.5°$	$270.0 \le \theta \le 330.0°$	$\tau = 100 \to 0\%$
D1:D2$_{D2}$	$63.0 \le \theta \le 96.5°$	$30.0 \le \theta \le 90.0°$	$\tau = 100 \to 0\%$
D2:D3$_{D3}$	$183.0 \le \theta \le 216.5°$	$150.0 \le \theta \le 210.0°$	$\tau = 100 \to 0\%$

Table 3.5 shows that as the source distance increases the angle range for the

attenuation region increases for each sensor. For source distances approaching the far

field, these angle regions limits equal the angles of the tangential lines described in **Table 3.4**.

3.3.3. Tunnel Region Shadowing

Based on the radial configuration of the sensor array and the dimension for each sensor, a physical gap exists between two of the sensors. This gap causes the third sensor to be exposed to additional gamma source angles outside the unity and attenuation region. In order to determine the shadowing coefficient associated with the tunnel region angles a similar approach can be used to find the shadowing coefficients as was used for determining the attenuation region. **Figure 3.11** illustrates an example of a tunnel gap respective to sensor D2 that was created by sensors D1 and D3.
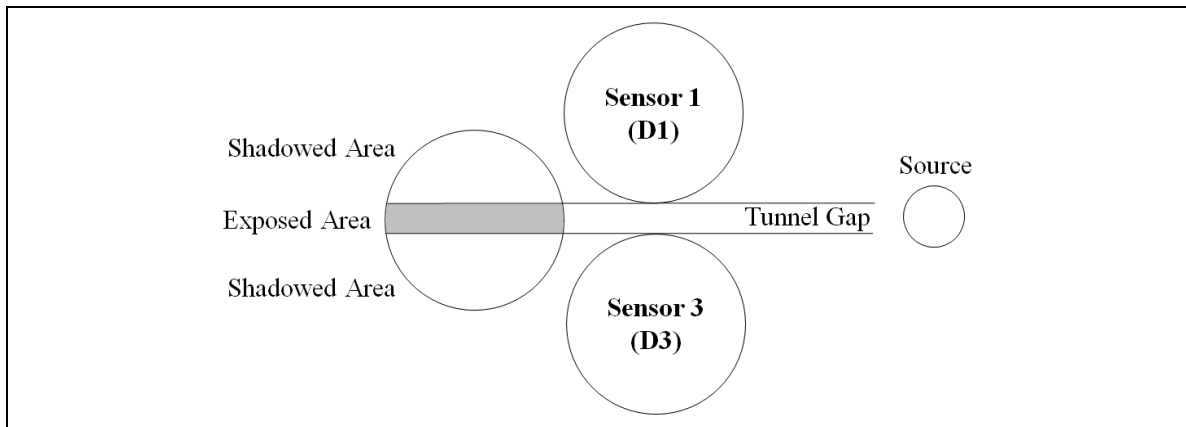
Figure 3.11: Sensor D2 Tunnel Gap Created by Sensor D1 and Sensor D3

In order to evaluate the exposed shaded area in **Figure 3.11** as the source rotates through the tunnel region, the width of the tunnel gap needs to first be calculated. This can be evaluated for D2 using **Equation 3.12**, the coordinates of sensors D1 and D3, and the sensor's radius.

$$\text{Tunnel Gap}_{D2} = \sqrt{(x_{D1} - x_{D3})^2 + (y_{D1} - y_{D3})^2} - 2r \qquad r = 1.0''$$

Equation 3.12: Tunnel Gap for Tunnel Region

Once the tunnel gap is evaluated, this value is used in conjunction with the same attenuation region equations for determining the segment area and shadowing coefficients. To determine θ_1 and θ_2 for the segment area equation, the exposed area in **Figure 3.11** is assumed to be the source angle range which produces the minimum amount of shadowing in this region. As the source rotates outside this angle range, this will follow the same curve as the attenuation region model until $\tau = 100\%$. The right triangles for θ_1 and θ_2 are determined by using one of the two incident vectors illustrated in **Figure 3.12**.
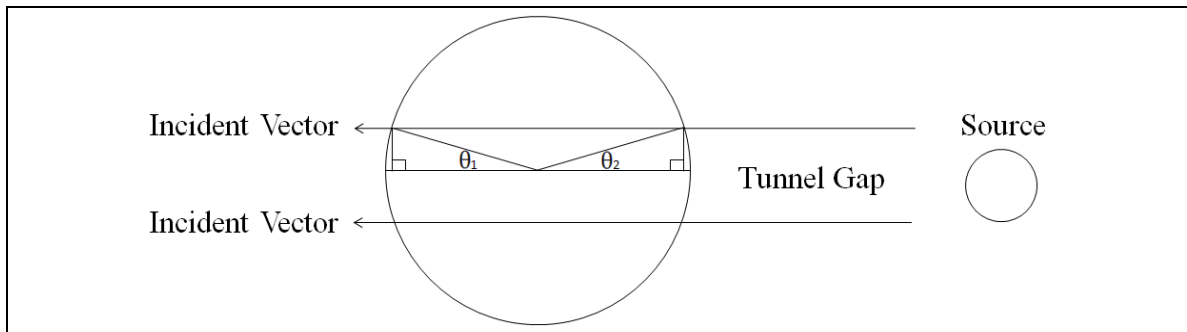
Figure 3.12: Right Triangles for Evaluating Segment Area

The right triangles illustrated in **Figure 3.12**, both θ_1 and θ_2 are equal. The hypotenuse of either triangle is equal to the sensor radius, and the opposite side is equal to one half the tunnel gap width calculated in **Equation 3.12**. Therefore, the inverse sine function can be used to calculate either of the angles. This angle result is then set equal to the other angle, and **Equation 3.9** is used to calculate the segment area. This value is then doubled to accommodate for the full shadowed area. The shadowing coefficient which represents the minimum possible shadowing for the tunnel region is calculated using **Equation 3.10**. The results are described in **Table 3.6**.

Table 3.6: Minimum Shadowing for a Given Sensor in the Tunnel Gap Region

Tunnel Gap	$\theta_1 = \theta_2$	$\theta_{Segment}$	Segment Area (x2)	Shadowing Coefficient
0.32"	9.2°	161.6°	1.25 x 2 = 2.5	80%

Table 3.6 shows that 80% represents the minimum possible shadowing that can occur in this region. Similar to the attenuation region, the shadow coefficient curve will follow the same curve illustrated in **Figure 3.8**, but begin at 80% instead of 0%, and continue until $\tau = 100\%$ when the gamma source exits the tunnel region. In order to calculate the near field and far field angle regions where $\tau = 80\%$, **Equation 3.13** is required to determine how the tunnel gap width maps onto the source longitude path.

$$\text{Angle Range} = \ 360/\left(\frac{2\pi r}{\text{Tunnel Gap}}\right)$$	r = Source Path Radius

Equation 3.13: Angle Range in the Tunnel Region for Minimum Shadowing

Using **Equation 3.13**, **Table 3.7** shows the full angle range of the tunnel region based on a source distance in the near field and a source distance in the extreme far field. These values represent the longitude angles for a given source distance where shadowing will begin to increase from $\tau = 80\%$, follow the curve in **Figure 3.8**, and reach the angle where $\tau = 100\%$.

Table 3.7: Sensor Angle Ranges for Tunnel Region Shadowing

Sensor	Angle Range $\tau = 80\%, r = 3$	Angle Range $\tau = 80\%, r = \infty$	Shadowing Coefficient	Final Angle Range Tunnel Region
D1	$237 < \theta < 240°$	$\theta = 240°$	$\tau = 80 \to 100\%$	r = 3 (Near) $216.5 < \theta < 263.5°$
	$240 < \theta < 243°$	$\theta = 240°$	$\tau = 100 \to 80\%$	r = ∞ (Far) $210 < \theta < 270°$
D2	$3 < \theta < 0°$	$\theta = 0°$	$\tau = 80 \to 100\%$	r = 3 (Near) $336.5 < \theta < 23.5°$
	$0 < \theta < 357°$	$\theta = 0°$	$\tau = 100 \to 80\%$	r = ∞ (Far) $330 < \theta < 30°$
D3	$117 < \theta < 120°$	$\theta = 120°$	$\tau = 80 \to 100\%$	r = 3 (Near) $96.5° < \theta < 143.5°$
	$120 < \theta < 123°$	$\theta = 120°$	$\tau = 100 \to 80\%$	r = ∞ (Far) $90° < \theta < 150°$

As the source distance increases the angle range for $\tau = 80\%$ decreases until both incident vectors are equal to the midpoint of the tunnel region. This is due to the tunnel gap width remaining constant even as the source path radius increases. This constant gap width becomes smaller in comparison to the longitude source path as the radius increases. Therefore, similar to the attenuation region, the angle range for the tunnel region also decreases with respect to the gamma source distance.

3.3.4. Dark Region Shadowing

Based on the radial configuration of the sensor array and the dimension for each sensor, sensors can exhibits maximum shielding at certain angle ranges. This angle region is defined as the dark region, and occurs when one sensor completely shadows one other sensor from the gamma source. This region is the last to be defined for each sensor because it can be determined by evaluating the difference in longitude angles between the tunnel region and the attenuation regions. Using the results from these regions, **Table 3.8** shows the full range of the dark region based on a source distance in the near field and a

source distance in the extreme far field. These values represent the longitude angles for a

given source distance where the shadowing coefficient is constant at $\tau = 100\%$.

Table 3.8: Sensor Angle Ranges for Dark Region Shadowing

Target Sensor	Sensor Shadow	Angle Range Near Field, r = 3.0"	Angle Range Far Field, r = ∞	Coefficient
D1	D2	$177.0 < \theta < 216.5°$	$\theta = 210°$	$\tau = 100\%$
	D3	$263.5 < \theta < 303.0°$	$\theta = 270°$	$\tau = 100\%$
D2	D1	$297.0 < \theta < 336.5°$	$\theta = 30°$	$\tau = 100\%$
	D3	$23.5 < \theta < 63.0°$	$\theta = 330°$	$\tau = 100\%$
D3	D1	$57 < \theta < 90°$	$\theta = 90°$	$\tau = 100\%$
	D2	$150 < \theta < 183°$	$\theta = 150°$	$\tau = 100\%$

Similar to the tunnel region, as the source distance increases the angle range of

the dark region decreases. Similar to the attenuation region, as the source distance

approaches the far field, the angles equal the tangential line angles in **Table 3.4**.

3.4. Cumulative Movement Model

Now that each of the regions in the shadowing model is understood, the effects of

each of these regions can be applied to the longitude and latitude directional models.

This will create a more accurate understanding of how the gamma event activity ratios for

each sensor will vary as a gamma source rotates at any latitude and longitude angle range

between $0 \le \theta < 360°$.

This is accomplished by multiplying the respective shadowing coefficient for each

longitude angle, depending on if the gamma source is in the near field or far field, by the

longitude activity ratio values for a given latitude value. As described in **Equation 3.14**,

the coefficient value to be multiplied should be $100\% - \tau$, since full shadowing should

null the activity value and no shadowing should maintain the original activity value.

$$a_i(\theta, \phi, \tau(\theta)) = (100\% - \tau(\theta)) \cdot a_i(\theta, \phi)$$

Equation 3.14: Application of Shadowing Coefficient to Longitude Model

Utilizing the angle ranges for each of the shadowing regions, the near field and far

field shadowing coefficients are illustrated in **Figure 3.13**.
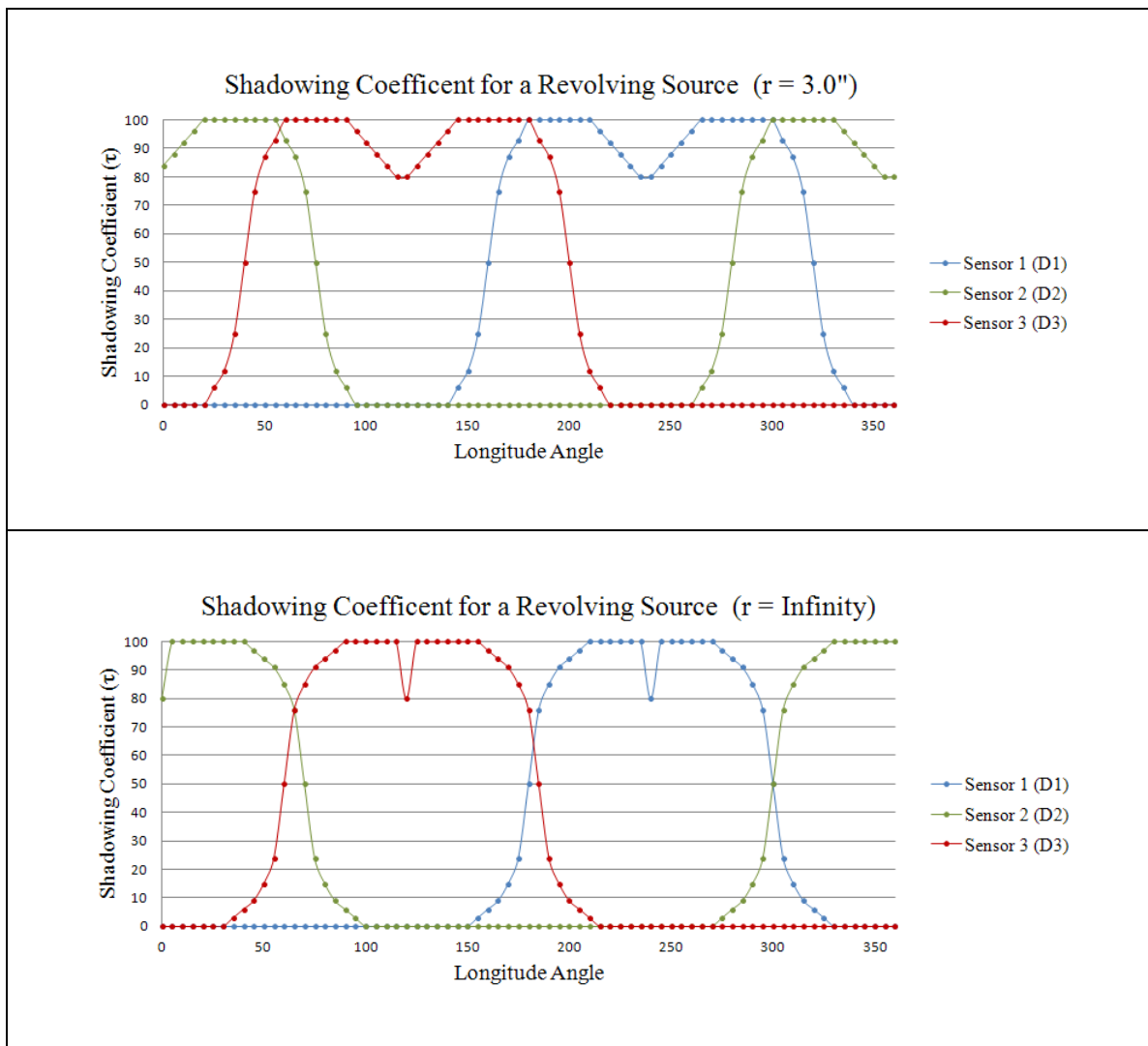
Figure 3.13: Near Field and Far Field Shadowing Coefficients

By applying the shadowing coefficient models in **Figure 3.13** to the activity

longitude directional model evaluated in **Figure 3.2**, a complete theoretical picture can be

drawn for how the activity should be affected as a gamma source rotates around the

sensor array. This is illustrated in **Figure 3.14** for both near field and far field source
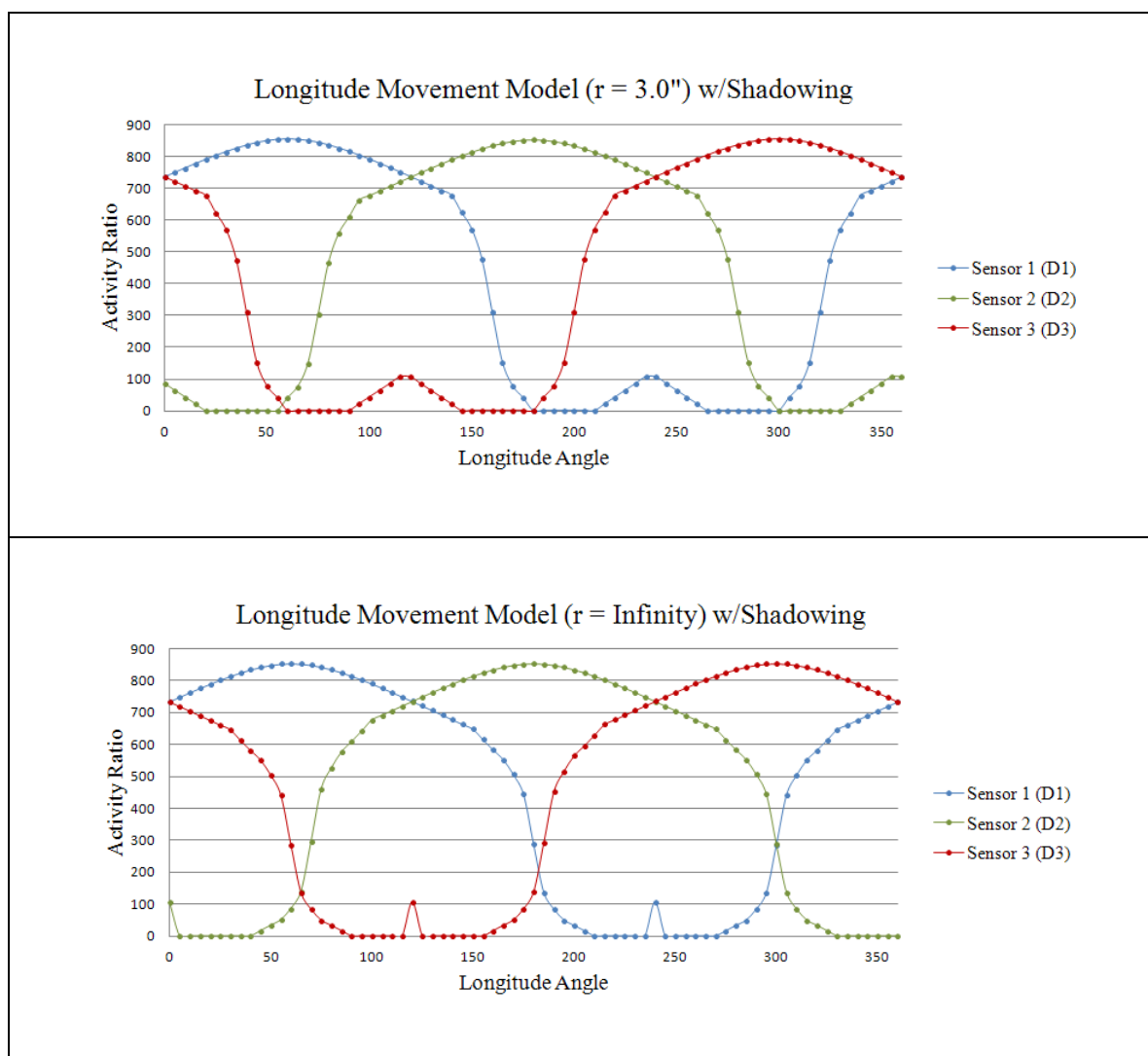
directions.

Figure 3.14: Apply Shadow Coefficients to Longitude Movement Model

The conclusion for the models in **Figure 3.14** is that there is distinct activity

ratios associated with each of the gamma source directions for both longitude and latitude

angles. This concept can be exploited by developing a set of algorithms that can run on

the computation subsystem to analyze the counts for a particular detection session, and

match the ratios to these models. This will be described in the next chapter which

describes the algorithms for implementing this determination mechanism for gamma source direction. In addition to the distinct activity ratios, the mathematical models express a significant symmetry that will also be exploited to minimize the algorithm detection complexities.

Figure 3.14 also illustrates that there are some structural differences between sources in the near field versus the far field. This is primarily due to the rate at which the source enters and exits both the attenuation region and tunnel region due to shadowing. Although this may be exploited in some usages, that particular evaluation is outside the scope of this thesis due to the fact that the sources used are too weak to gather data at relevant far field distances.

Chapter 4: Algorithm Development and Testing

The mathematical models described in the previous chapter provide a framework that can be used to detect the direction of a gamma source. In order to validate these models with the GRDS, a set of algorithms need to be developed for the computation subsystem which will process the results for a given detection session. A detection session is triggered by the specific gamma detection event capabilities of the GRDS, and completes when the counts reach a certain threshold within a target energy range. These count thresholds are predefined for each target gamma source, and are dependent on three areas.

1. The number of counts for a given energy range is large enough for the detection algorithms to work effectively.

2. The amount of time required to reach the count thresholds for each target gamma source does not exceed a timeout.

3. A dominant peak exists within a certain energy range to provide confidence that a specific source exists.

After a detection event is triggered the sensor array begins a detection session by first clearing all previous counts, and then begins to constantly collect data for a given period of time, or until a count threshold is reached. The GRDS measures each photoelectron particle that is generated from each of the sensors in the array. The digital value from each sensor's ADC is then compared to the energy ranges for each of the 256 buckets. If the energy value falls within one of these ranges, that particular bucket counter is incremented. When the detection session has ended, based on either a predefined timeout or minimum count being reached, the bucket count values for each of

the sensors are read and processed by the detection algorithms. The result of these algorithms identify if any of the target gamma sources are present, and determines the respective longitude and latitude direction of those sources.

4.1.   Software Emulation Tool

The detection algorithms were developed using a software emulation tool running on a client PC and based on C# language. Since the GRDS computation subsystem uses a custom MSP430 microprocessor variant (NSP430), there are not many intuitive tools to develop, validate, and debug the capability and performance of this new set of algorithms. In addition, simulation is a challenge with the GRDS because the computation subsystem memory size is limited and creates a challenge to store various detection sessions for testing. Therefore, it was imperative to develop a client PC software tool that had both an intuitive graphical user interface for visual validation and debug, and also allowed for quick simulation of many detection sessions. A screenshot of this tool is illustrated in **Figure 4.1**.
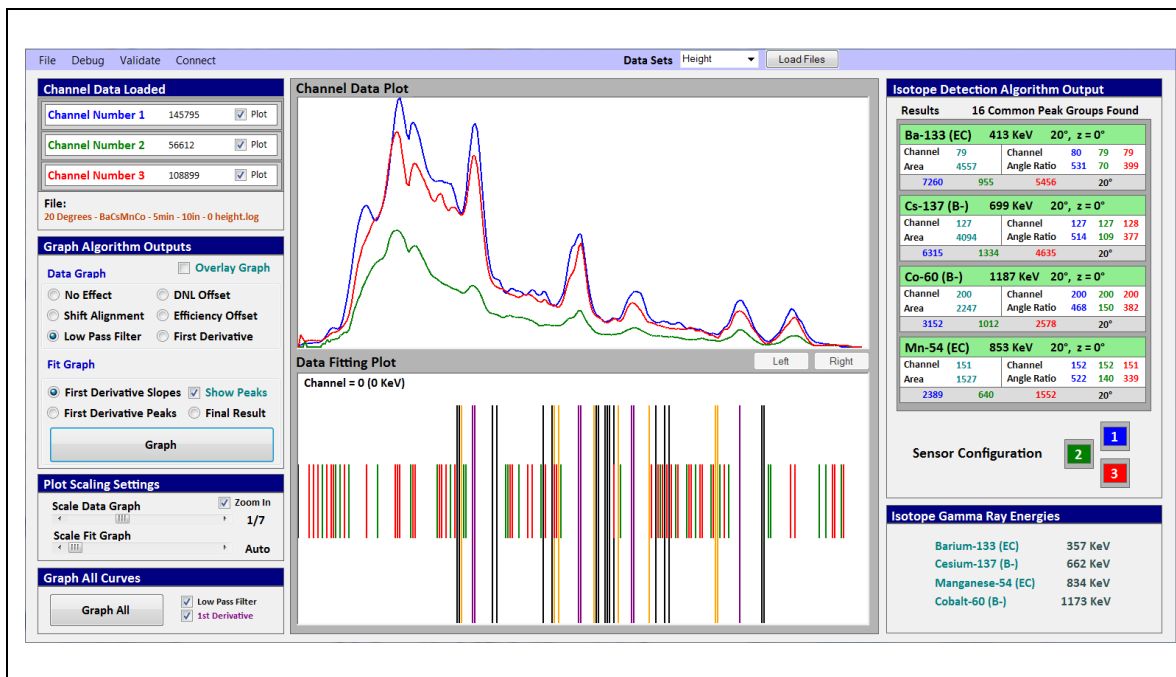
Figure 4.1: Software Emulation Tool Test Environment

In order for the tool to emulate detection sessions many datasets were initially collected using the GRDS. The datasets contained the 256 bucket values for each of the three sensors and were collected with a specific gamma source configuration and a specific detection session time. These final values were then read over USB from the GRDS to the client PC and then stored into text files which could be read by the tool. Simulation was a fundamental requirement because the gamma sources used for development and testing were very weak radiation sources (1uCi), and based on the respective count thresholds, could take several minutes to collect enough data to create a reasonable detection session. By storing the results of various detection sessions into text files, this enabled a simulation method for determining the algorithm results for any source configuration very quickly. Once the algorithms were validated using this tool, the C# code was ported to C language, compiled, and flashed onto the NSP430.

4.2. Detection Algorithm

The algorithms for gamma isotope identification and source directional

determination are broken up into a series of processing phases. These phases are both

used to determine if the minimum number of counts for a given energy range has been

reached and used to process the results after a detection session has completed. In each

case, the raw data values for each of the sensor buckets are copied to a 3 x 256 matrix in

RAM for processing. These data values are first interpolated for each sensor to remove

any zeros between adjacent buckets. These zeros can either occur because no energy at

that range was measured, or a bucket value was shadowed by the analog noise error of

the ADC between adjacent buckets. Therefore, these shadowed buckets are assigned a

value based on the non-zero values of the adjacent buckets. This ensures each curve

provides a reasonable smooth transition between buckets that can be processed more

efficiently by the algorithms. The linear interpolation function for bucket values equal to

zero is defined in **Equation 4.1**.

$$\text{Bucket Value[i]}_{\text{Interpolate}} = \left(\frac{\text{Bucket Value[i − Previous]} + \text{ Bucket Value[i + Next]}}{(i + \text{Next}) - (i - \text{Previous})} \right)$$

Equation 4.1: Linear Interpolation Function for Buckets Equal to Zero

The index values for previous and next in **Equation 4.1** are determined based on

which adjacent buckets have a non-zero counter value. These values define the bucket

and index values used to calculate the slope of the linear interpolation function. This

function is then applied to all buckets in between these index values which have a zero

counter value to calculate the new interpolated value. The code required to implement

this interpolation function is defined in **Code 4.1**.

```
for (sensor = 0; sensor < 3; sensor++) {
    for (bucket = 0; bucket < 256; bucket ++) {
        if (OriginalData[bucket] == 0) {
            int j = bucket;
            while (OriginalData[j] == 0) {
                j = j + 1;  //locate next bucket that is non-zero
            }
            slope = (OriginalData[j] – OriginalData[bucket – 1]) / (j – bucket – 1)
            OriginalData[bucket] = OriginalData[bucket – 1] + slope;
        }
    }
}
```

Code 4.1: Linear Interpolation Function

4.2.1. Data Calibration Phase

The first processing phase after the raw data has been copied to the 3 x 256 matrix and interpolated is the data calibration phase. This phase cleans up the data by removing any detector or computation subsystem inconsistencies when executing the detection algorithms [4]. This phase is separated into three areas.

1. **Differential Nonlinearity Offset:** This calibration is used to equalize the digital output fluctuations between each of the sensor's ADC for a given analog value. If this calibration is not performed correctly, the analog energy value for each sensor will be converted incorrectly and placed into the wrong digital bucket.

2. **Data Alignment:** In this calibration process the energy values for each of the sensors is aligned. This may require a left shift or right shift for certain bucket energy ranges. If this calibration is not performed, a bucket at a particular energy value of one sensor will not be associated with the same bucket and energy value of the other sensors.

3. **Sensor Efficiency:** This calibration is used to correct any sensitivity inconsistencies with respect to each of the scintillator sensor units. Even though the three sensors are from the same manufacturer and the same part number, differences can exist with respect to the sensor efficiencies for particular energy ranges.   If this calibration is not performed, the number of counts detected for each energy range will be higher or lower for each sensor at the same source distance and incident vector.

Differential nonlinearity (DNL) offset accommodates how much two adjacent digital coded analog values deviate from the ideal 1LSB (least significant bit) step value. This can only be evaluated using an analog voltage source, a voltmeter, and verifying the output digital value from the ADC. By stepping through the analog voltage range of the ADC for each sensor channel and verifying the respective digital output, this non-linearity can be evaluated for each bucket.

In order to program the DNL offset, an independent 3 x 256 matrix is required to represent each bucket for each sensor. To decrease or increase the analog offset for a digital value, a value relative to 256 needs to be assigned to each bucket. During calibration, the bucket value will be adjusted based on each respective DNL offset value using **Equation 4.2**.

$$\text{Bucket Value}_{\text{DNL Offset}} = \text{Bucket Value}_{\text{Interpolate}} \cdot \left(\frac{\text{DNL Offset Value}}{256}\right)$$

Equation 4.2: DNL Offset Value Calculation

The reason that 256 was chosen as the scaling denominator is because it is straightforward to divide by 256 using the NSP430 and a bitwise left-shift operator.

Data alignment pertains to how the energy range for each of the sensor's 256

buckets aligns with the 256 buckets for the other two sensors. Bucket energy ranges can

be adjusted by assigning a positive or negative shift value for a given energy range. If the

bucket index needs to be shifted to a lower energy range a positive shift value is assigned.

If the bucket index needs to be shifted to a higher energy range a negative shift value is

assigned. Similar to sensor efficiency, this can be evaluated using the software tool. By

plotting the output for a multiple gamma source detection session, multiple distinct peaks

should be apparent. This plot will make it straightforward to quantify the alignment for

each of these peaks with respect to each sensor's output.

Depending on the number of detected gamma sources to be supported, and the

energy ranges of those sources, some care should be taken regarding the integrity of the

data between peaks. For example, it is acceptable to shift or overwrite the bucket data

for a given energy range to a new energy range, as long as the overwritten data is not

within another target energy range. The energy range to be shifted will create an

alignment set. Each alignment set will consist of a minimum bucket index value, a

maximum bucket index value, and a left or right shift value. This calculation is shown in

Equation 4.3.

$$\text{Bucket Value}[i - \text{Shift}]_{\text{Alignment}} = \text{Bucket Value}_{\text{DNL Offset}}[\, i \,]$$

Equation 4.3: Data Alignment Value Calculation

The sensor efficiency inconsistencies are resolved through two techniques. The

first technique is considered a course correction, and utilizes the findings from the

directional models developed in the previous chapter describing latitude movement. The

model showed that when gamma sources are at a latitude angle of either $\phi = 90°$ or

$\phi = 270°$ the energy range count value for each sensor bucket should be the same. By taking measurements for each of the target sources in either of these directions, the count output can be compared using the software tool to determine the inconsistencies between the sensitivity of each sensor. If at any energy range the count values are not the same then the efficiency value for those buckets needs to be adjusted. It is recommended that $\phi = 270°$ (below sensor array) is used because of the GRDS design. At this angle the scintillator crystal has a line of sight to the gamma source compared to $\phi = 90°$ (above sensor array).

The second technique involves fine tuning the efficiency value evaluated in the course correction technique. This technique again utilizes the findings from the directional models in the previous chapter. By evaluating the longitude angle model in **Figure 3.5**, there exist certain sensor array identities that can be created for various source angles when $\phi \neq 90°$ or $\phi \neq 270°$. These identities are described in **Table 4.1**.

Table 4.1: Fine Correction Identity for Sensor Efficiency

Source Angle	Identity 1	Identity 2
$\theta = 0°$	D1 Count Ratio = D3 Count Ratio	D2 Count Ratio at Minimum
$\theta = 60°$	D2 Count Ratio = D3 Count Ratio	D1 Count Ratio at Maximum
$\theta = 120°$	D1 Count Ratio = D2 Count Ratio	D3 Count Ratio at Minimum
$\theta = 180°$	D1 Count Ratio = D3 Count Ratio	D2 Count Ratio at Maximum
$\theta = 240°$	D2 Count Ratio = D3 Count Ratio	D1 Count Ratio at Minimum
$\theta = 300°$	D1 Count Ratio = D2 Count Ratio	D3 Count Ratio at Maximum

Unlike DNL offset, these two techniques for sensor efficiency are not applied until after the data has been processed through a low pass filter. As will be described later in this chapter, the low pass filter output is what is used to determine peak energy,

and therefore must meet the efficiency criteria. The low pass filter output is also what is used to create another independent 3 x 256 matrix to represent an efficiency value for each bucket index and for each sensor. Similar to DNL offset, in order to decrease or increase the efficiency a value relative to 256 needs to be assigned to each bucket.

4.2.2. Applying Data Calibration Function

Once the calibration values are determined, there are two functions needed to apply the data calibration to the raw and interpolated data copied into memory. The first function will apply the sensor DNL offset and the second function will apply the data alignment. The efficiency matrix will not get applied until after the low pass filter is processed. The first function is implemented by looping through all the buckets for a given sensor and multiplying the corresponding value in the DNL offset matrix according to **Equation 4.2.** The code required to implement this first function is described in **Code 4.2**.

```
for (sensor = 0; sensor < 3; sensor++) {
   for (bucket = 0; bucket < 256; bucket ++) {
      DNLOffsetData[sensor][bucket] = OriginalData[sensor][bucket] *
         (DNLOffset[sensor][bucket] / 256);
   }
}
```

Code 4.2: Apply DNL Offset Function

The second function for data alignment is implemented by again looping through all the buckets for a given sensor. If the bucket falls within the energy range to be aligned, it is shifted based on that value. The code required to implement this second function is described in **Code 4.3**.

```
for (sensor = 0; sensor < 3; sensor++) {
    for (bucket = 0; bucket < 256; bucket ++) {
        for (j = 0 ; j < AlignmentSets[sensor].Count; j++) {
            MinValue = AlignmentSets[sensor][j].MinBucketIndex;
            MaxValue = AlignmentSets[sensor][j].MaxBucketIndex;
            ShiftValue = AlignmentSets[sensor][j].ShiftValue;
            if (bucket >= MinValue && bucket <= MaxValue) {
                CalibratedData[sensor][bucket] =
                    DNLOffsetData[sensor][bucket + ShiftValue];
            }
        }
    }
}
```

Code 4.3: Apply Data Alignment Function

Regarding **Code 4.3**, and depending on the energy range and shift value,

additional care needs to be taken to ensure that array indexing does not index elements

outside the 256 bucket memory boundaries. This can occur if the bucket subtracted from

the shift value is less than 0, or if the bucket added to the shift value is greater than 255.

To prevent this from occurring, an additional check for these conditions needs to be

placed into the function.

4.2.3. Applying Low Pass Filter Function

The next phase of the algorithm implements a low pass filter on the calibrated

data. The reason for this phase is that the data collected during a detection session can

have a significant number of high frequency attributes in the output which will make it

more difficult to identify peak components. This filter will smooth out the data and help

improve the efficiency of the follow on phases in the algorithm. The low pass filter that

was chosen was a triangle notch filter [5]. This is applied to the bucket output for each

sensor using the formula described in **Equation 4.4**.

$$\text{LowPassFilter[bucket]} = \frac{1}{9} \sum_{k=0}^{4} \text{CalibratedData[bucket} + (k-2)] \cdot w(k)$$

$$w(k)_{k:0 \to 4} = \{1, 2, 3, 2, 1\}$$

Equation 4.4: Triangle Notch Low Pass Filter Formula

The low pass filter is implemented into the algorithm by looping through all the

buckets for a given sensor and applying **Equation 4.4**. The code required to implement

this function is described in **Code 4.4**.

```
for (sensor = 0; sensor < 3; sensor ++) {
    for (bucket = 2; bucket < 254; bucket ++) {
        LowPassFilter[sensor][bucket] = (1/9) * (1 * CalibratedData[bucket - 2] +
            2 * CalibratedData[bucket - 1] + 3 * CalibratedData[bucket]  +
                2 * CalibratedData[bucket + 1] + 1 * CalibratedData[bucket + 2]);
    }
}
```

Code 4.4: Apply Low Pass Filter Function

The result of the low pass filter will yield a smooth curve, and due to the

minimum counts required to process a detection session, should also yield distinct peaks

in the target energy ranges. An example of one sensor's original bucket data and

respective low pass filter output is illustrated in **Figure 4.2**.
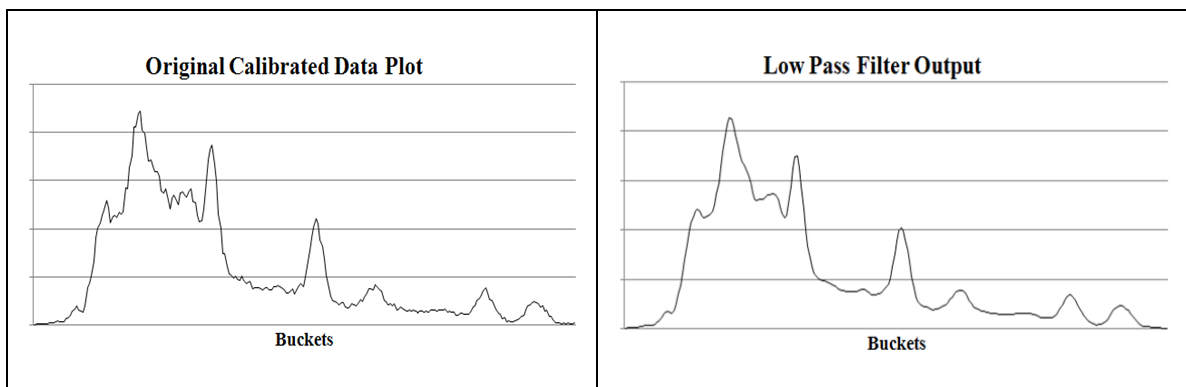
Figure 4.2: Application of the Low Pass Filter Function

Similar to the data alignment function, there exists a boundary condition for the

low pass filter function defined in **Code 4.4**. Since the low pass filter requires data

indexing of at least two buckets in either direction from the target bucket, this boundary

condition will exist at bucket index 1 and at bucket index 254 for each sensor. The

function can avoid this condition by only performing the low pass filter on bucket index 2

through 253 instead of index 0 through 255, and then setting values outside this range to

zero. This is a non-issue because any peaks created by the target gamma sources will be

within these bucket index values.

4.2.4. Applying Efficiency

As was described in the data calibration phase, an efficiency matrix needs to be

applied to the low pass filter to accommodate for any mismatch in sensitivities between

sensors. Each of these efficiency values will be input into **Equation 4.5** to determine the

final low pass filter value before proceeding onto the rest of the detection algorithm.

$$\text{EfficiencyLPF[bucket]} = \text{LowPassFilter[bucket]} \cdot \left(\frac{\text{EfficiencyValue[bucket]}}{256} \right)$$

Equation 4.5: Efficiency Value Calculation

The efficiency matrix needs to be calculated in advance, and although the second

technique for fine tuning requires detailed evaluation, the first technique for course

correction can be calculated through a very straightforward method. This involves

comparing the low pass filter result of sources at $\phi = 270°$ and using the function

described in **Code 4.5**.

```
for (bucket = 0; bucket < 256; bucket ++) {
    MaxValue = Math.Max(LowPassFilter[0][bucket], LowPassFilter[1][bucket],
        LowPassFilter[2][bucket]);  //compare each sensor bucket output
    for (sensor = 0; sensor < 3; sensor ++) {
        SensorValue = LowPassFilter[sensor][bucket];
        if (SensorValue == 0) {
            EfficiencyValue[sensor][bucket] = 0;
        }
        else if (SensorValue <= MaxValue) {
            EfficiencyValue[sensor][bucket] =
                (((MaxValue – SensorValue) / SensorValue) * 256) + 256;
        }
        else if (SensorValue > MaxValue) {
            EfficiencyValue[sensor][bucket] =
                256 – (((SensorValue – MaxValue) / SensorValue) * 256);
        }
    }
}
```

Code 4.5: Course Correction Efficiency Value Calculation

Once the efficiency matrix has been determined, a function similar to **Code 4.2**

for applying DNL offset is applied to the low pass filter output for efficiency. The result

of this function produces data which now considers all three of the calibration areas. This

is described in **Code 4.6**.

```
for (sensor = 0; sensor < 3; sensor++) {
    for (bucket = 0; bucket < 256; bucket ++) {
        EfficienyLPF[sensor][bucket] = LowPassFilter[sensor][bucket] *
            (EfficiencyValue[sensor][bucket] / 256);
    }
}
```

Code 4.6: Apply Efficiency Function

4.2.5. Applying First Derivative Function

In the next phases the algorithm begins to identify the relevant energy peaks in

each sensor's output [5]. This is accomplished by first evaluating the first derivative

curves for each sensor's low pass filter output.   Any potential peaks are identified by

locating the zero crossing points in the first derivate output. This corresponds to the low

pass filter output where the slope changes between positive to negative or negative to

positive. These values are then used to identify the three points which make up a peak.

These points are left peak base point, peak point, and right peak base point. These are

illustrated in **Figure 4.3**.
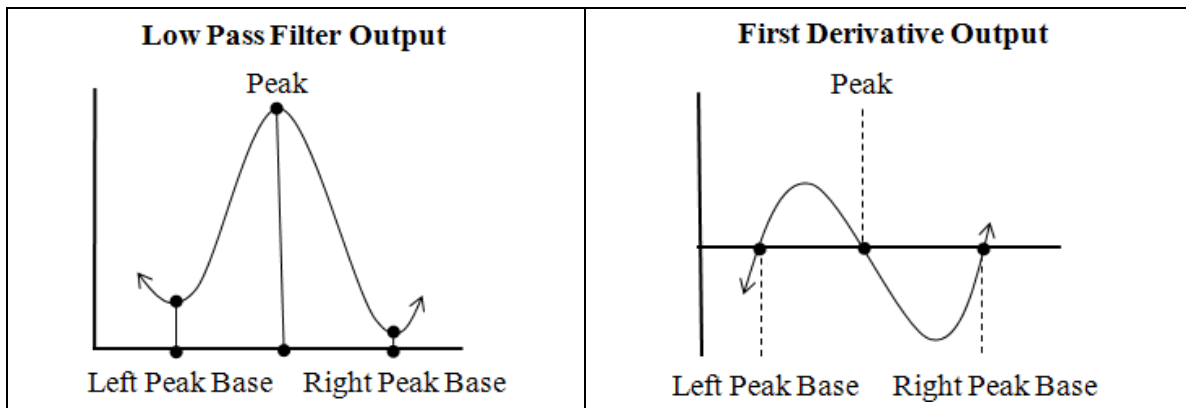
Figure 4.3: Peak Points for Low Pass Filter and First Derivate Outputs

The first derivative is the primary reason for having the counts at least at a

minimum value before processing a detection session. If the counts are not at a minimum

value, then the first derivate curve can tend to oscillate about the peak base points. This

can cause the left peak base and right peak base points to become less apparent and more

difficult to identify. The first derivative is based on a bucket index delta of two with

respect to the low power filter output, and is defined in **Equation 4.6**.

$$\text{FirstDerivative[bucket]} = \frac{\text{EfficiencyLPF[bucket]} - \text{EfficiencyLPF[bucket} + 1]}{2}$$

Equation 4.6: First Derivative of the Low Pass Filter Output

The first derivative is implemented into the algorithm by looping through all the

bucket values for a given sensor's low pass filter output and applying **Equation 4.6**. The

code required to implement this function is described in **Code 4.7**.

```
for (sensor = 0; sensor < 3; sensor ++) {
    for (bucket = 0; bucket < 255; bucket ++) {
        FirstDerivative[sensor][bucket] =
            (EfficiencyLPF[sensor][bucket] + EfficiencyLPF[sensor][bucket + 1]) / 2;
    }
}
```

Code 4.7: First Derivative Function

The index delta chosen for this first derivate function may create a boundary

condition which may require a check similar to what was described for the low pass filter.

The result of **Code 4.7** will create a 256 element array for each sensor that contains the

low pass filter slope value at every bucket index.

4.2.6. Identify Relevant Peaks

In this phase relevant peaks in each sensor's output are identified. This requires

two functions to compare each sensor's first derivative output values with the explicit

peak point pattern illustrated in **Figure 4.3**. This pattern is based on the three conditions

described in **Table 4.2** and must occur in a strict order.

Condition Order	Peak Point	Qualifier	Threshold
1	Left Peak Base	Negative to Positive	Slope > 1.0
2	Peak	Positive to Negative	None
3	Right Peak Base	Negative to Positive	Slope > 1.0

Table 4.2: Ordered Conditions to Identify Relevant Peaks

A threshold for condition 1 and 3 are assigned a second order qualifier and based

on the minimum counts and index delta used for the first derivative. This threshold helps

to ensure the left peak base point is not identified at a too low energy level and the right

peak base point is not identified at a too high energy level. This would result in a peak

that is wider than necessary. The varying width of the peak base points are a

characteristic of the sensor error. The ideal sensor would create a zero width peak, or

impulse, at each gamma source energy value, but due to this error a gamma source can be

measured within a given energy range. The threshold is illustrated in **Figure 4.4**.
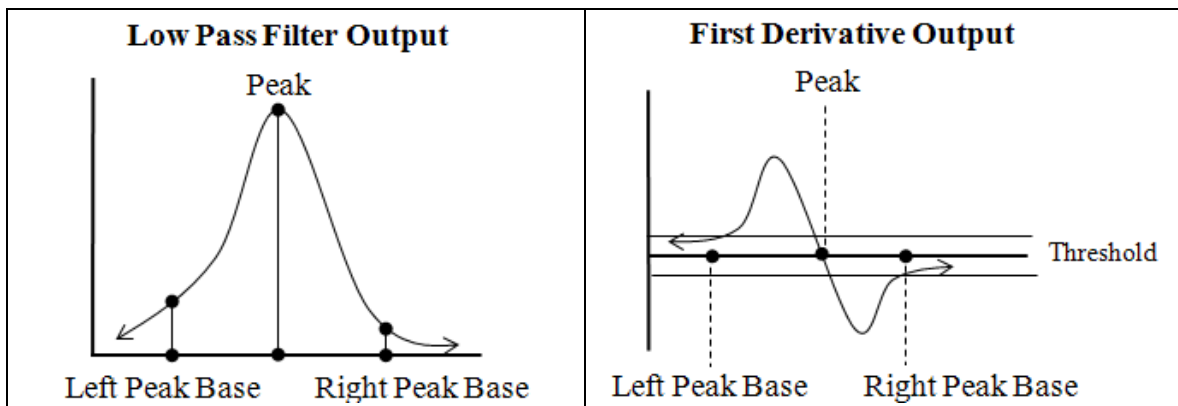
Figure 4.4: First Derivative Peak Points with Threshold

The first function for relevant peak detection implements a condition and

threshold filter on the first derivate output based on the descriptions in **Table 4.2**. The

output of this filter identifies for each bucket value which of these conditions and

thresholds have been met. This is implemented into the algorithm by looping through all

the bucket values for a given sensor's first derivate output and assigning a fixed value

based on the met conditions. The code required to implement this function is described

in **Code 4.8**.

```
for (sensor = 0; sensor < 3; sensor ++) {
    for (bucket = 0; bucket < 256; bucket ++) {
        ConditionFilter[sensor][bucket] = 2; //No condition met
        if (Math.Abs(FirstDerivative[sensor][bucket]) < Threshold) {
            ConditionFilter[sensor][bucket] = 0; //Left Peak Base or Right Peak Base point.
        }
        else if (FirstDerivative[sensor][bucket] < 0 & FirstDerivative[sensor][bucket + 1] > 0) {
            ConditionFilter[sensor][bucket] = 0; //Left Peak Base or Right Peak Base point.
        }
        if (FirstDerivative[sensor][bucket] > 0 & FirstDerivative[sensor][bucket + 1] < 0) {
            ConditionFilter[sensor][bucket] = 1; //Peak point, overwrites threshold if condition met
        }
    }
}
```

Code 4.8: Condition and Threshold Filter Function

In **Code 4.8,** the peak point conditions only compare one index value above a target bucket index. There may be circumstances which require the comparison of index values above more than one bucket index. For example, this may occur for peak points where slope values in this range could span across three bucket index values instead of two. Instead of strictly comparing a positive to negative value across two buckets, the slope values could span from a positive value to zero and zero to a negative value requiring a three bucket index check.

The second function for relevant peak detection parses the output of the condition and threshold filter for each sensor. This function compares the filter output to the strict condition order described in **Table 4.2**, and outputs an array of relevant peak structures. The code required to implement this function is described in **Code 4.9.**

```
for (sensor = 0; sensor < 3; sensor ++) {
    count = 0; //number of peaks identified for each sensor
    for (bucket = 0; bucket < 256; bucket++) {
        //code to locate first bucket that has ConditionFilter[sensor][bucket] = 0
        //Condition 1
        //from this bucket loop through until ConditionFilter[sensor][bucket] not equal to 0
        PeakStructure.LeftPeakBase = bucket;
        //Condition 2
        //from Condition 1 bucket, loop through until ConditionFilter[sensor][bucket] equals 1
        PeakStructure.Peak = bucket;
        //Condition 3
        //from Condition 2 bucket loop through until ConditionFilter[sensor][bucket] equals 0
        PeakStructure.RightPeakBase = bucket;
        //IF all of the conditions are met in the correct order, THEN
            PeakArray[count] = PeakStructure;
            count = count + 1;
        //IF any condition is not met in the correct order, THEN
        //set 'for' loop bucket value to the value of last condition loop value and start again
    }
}
```

Code 4.9: Relevant Peak Detector Function

Once the relevant peak structures have been identified in **Code 4.9**, the next step

is to determine the total peak energy for each of the peak structures. This total peak

energy will assign a weight value for each peak which will determine relevance. In order

to calculate this total peak energy value, integration needs to be performed using both the

count values from the low pass filter output and the peak structures identified from **Code**

4.9. There are two considerations to keep in mind when performing this integration.

The first consideration, as discussed previously, is the detection error for each

sensor. This means that when a gamma source with a specific energy hits the scintillator

crystal, it could be converted into a photon with a range of energy values. In this case

the error range for each sensor is +/-3% for a given energy value. Therefore, if the peak

base points describe a peak width that is greater than this error, an attenuation filter is

applied. For bucket values inside the error window, the assumed attenuation will be zero,

but for buckets outside this error window, the attenuation will increase linearly from zero

to 100%. This linearity will be based on the bucket values from the error window to the

peak base points. The attenuation filter is illustrated in **Figure 4.5**.
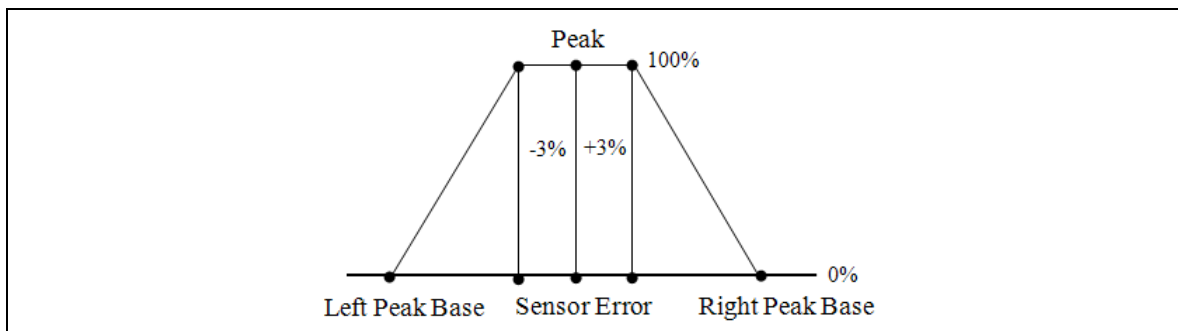
Figure 4.5: Attenuation Filter for Peak Energy Integration

The second consideration is the gamma energy offset [5] which takes into account

atomic interactions when the gamma ray hits the scintillator crystal. These interactions,

such as Compton scattering, can cause photons at a lower energy range to be emitted that

are not the energy value of the target gamma source. This can cause the count values of

certain buckets to be synthetically higher. This occurs if there is more than one gamma

source present during a detection session and one of those sources has a higher energy

value. Therefore these additional synthetic counts for a given energy range need to be

removed. There are two methods which can be utilized using the peak base points

illustrated in **Figure 4.6**.
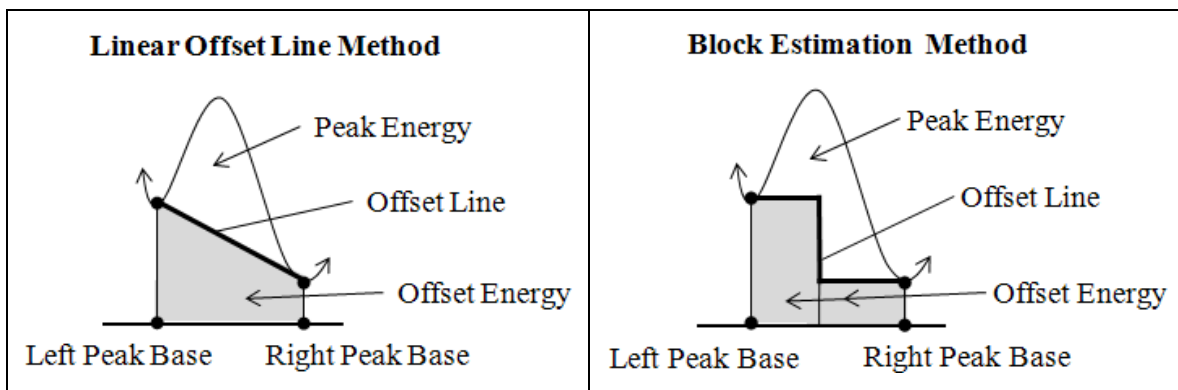
Figure 4.6: Methods for Removing Offset Energy due to Atomic Interactions

The first method describes a linear offset model which defines a slope line equation from the peak base points and low pass filter values. To calculate the total peak energy, each of these low pass filter values within the peak is deducted from the slope line value at each bucket index. This linear equation definition is described in **Equation 4.7**.

$$slope = \frac{RightPeakBase_{EfficiencyLPF} - LeftPeakBase_{EfficiencyLPF}}{RightPeakBase_{BucketIndex} - LeftPeakBase_{BucketIndex}}$$

$$y_{Intercept} = LeftPeakBase_{EfficiencyLPF} - (slope * LeftPeakBase_{BucketIndex})$$

$$PeakOffsetEnergy = (slope * Bucket_{Index}) + y_{Intercept}$$

Equation 4.7: First Offset Energy Removal Method

The second method describes an estimation of the linear offset model by defining two distinct offset regions to be removed. Instead of subtracting the slope value at each point during integration, a static value is deducted at each point based on the bucket's offset region. The static value for the first region is defined as the low pass filter value at the left peak base point, and is deducted from all bucket values between the left peak base point and the peak point. The static value for the second region is defined as the low pass filter value at the right peak base point, and is deducted from all bucket values between the peak point and the right peak base point.

Of the two offset removal methods, the first method was chosen for removing the peak offset energy because it evaluates the peak offset in the most detail. This method requires that a slope value be calculated for each bucket compared to removing a static value in the second method. Therefore, by using the attenuation filter and first peak

offset method, an equation can be created to determine the true energy for any given

peak. This equation is defined in **Equation 4.8**.

$$\text{Peak Energy} = \left(\int \text{EfficiencyLPF}_{\text{Bucket}} - \text{PeakOffsetEnergy} \right) \cdot \text{AttenuationStructure}$$

Equation 4.8: Peak Energy Integration

      The peak energy integration is implemented into the algorithm by looping through

all the peak structures and applying **Equation 4.8**. This peak energy value can then be

stored as a weighting value for each peak structure. The code required to implement this

function is described in **Code 4.10**.

```
foreach (PeakStructure ps in PeakArray) { //ps = Sensor Peak Structures
   PeakEnergy = 0;
   slope = (EfficiencyLPF[ps.RightPeakBase] – EfficiencyLPF[ps.LeftPeakBase]) /
              (ps.RightPeakBase – ps.LeftPeakBase);
   y_intercept = EfficiencyLPF[ps.LeftPeakBase] – (slope * ps.LeftPeakBase);
   for (i = ps.LeftPeakBase <= ps.RightPeakBase; i++) {
      PeakOffsetEnergy = (slope * i) + y_intercept;
      BucketEnergy = (EfficiencyLPF[i] -  PeakOffsetEnergy) * AttenuationFilter(ps, i));
      PeakEnergy =  PeakEnergy + BucketEnergy
   }
   ps.Energy = PeakEnergy;
}
```

Code 4.10: Peak Energy Integration Function

      As part of **Code 4.10** the attenuation filter is implemented by comparing the peak

structures to the sensor error and respective peak base points and then applying the

structure in **Figure 4.5**. Based on a sensor error of +/- 3% and 256 buckets for each

sensor, the 3% error would equate to 8 buckets. The code required to implement this

filter is described in **Code 4.11**.

```
//'i' equals for loop bucket value passed from integration function
//'ps' equal PeakStructure value pass from integration function
AttenuationLeftSlope = (1 / (ps.Peak – 8 – ps.LeftPeakBase); //slope from 100% - 0%
AttenuationRightSlope = (1/ (ps.RightPeakBase – ps.Peak + 8);  //slope from 100% - 0%
if (i >= (ps.Peak – 8) && i <= (ps.Peak + 8)) {
    return 1;  //no attenuation
}
else if (i < (ps.Peak – 8)) {
    return = AttenuationLeftSlope * (i – LeftPeakBase);
}
else if (i > (ps.Peak + 8)) {
    return = AttenuationRightSlope * (RightPeakBase – i);
}
```

Code 4.11: Attenuation Filter Function

Once the peak structures are identified and a peak energy or relevance has been

assigned, a sorting of the peak structures is done based on the peak energy. This sort

arranges each sensor's peak structures in a descending order based on the peak energy,

and is accomplished using the bubble sort function described in **Code 4.12**.

```
// count equals the number of peak structures identified for each sensor
for (sensor = 0; sensor < 3; sensor ++) {
    for (i = count - 1; i >= 0; i--) {
        for (j = 1; j <= i; j++) {
            ps1 = PeakArray[sensor][j - 1];
            ps2 = PeakArray[sensor][j];
            if (ps1.Energy < ps2.Energy) {
                ;swap the locations of PeakStructure at index "j-1" and "j"
                PeakArray[sensor][j - 1] = ps2;
                PeakArray[sensor][j] = ps1;
            }
        }
    }
}
```

Code 4.12: Peak Structure Weight Value Bubble Sorting Function

After executing **Code 4.12**, the peak structures are sorted based on relevance for

each sensor. The next phase in the algorithm compares all peak structures to find

commonalities in peaks detected between all three sensors.

4.2.7. Identify Gamma Sources Based on Common Peaks

One of the primary advantages of having an array of sensors versus just one sensor is that it produces multiple perspectives. These perspectives, represented as a set of peak structures, can be compared across all three sensors to ensure confidence in the list of identified peaks [4]. Therefore, the assumption during this phase, and to help avoid false positive detections, is that all sensors need to identify the same peak structure before the peak is considered a relevant detection. There are approaches which could involve partial detection with one or two of the sensors detecting a common peak structure, but that is outside the scope of this evaluation. In addition, it would not be possible to calculate direction according to the mathematical models described previously.

After the peak structures have been sorted, another search is completed to identify which peak structures were found by all three sensors within a given threshold. This threshold is only relative to the peak point of the peak structure, and is dependent on the quality of the data alignment step in the calibration phase. The common peaks function is implemented by looping through all the peak structures for each sensor and comparing the peak value. If the peak value is within a given threshold for all three sensors, those three peak structures are added to the common peaks structure list. In addition to this list, the average bucket index value and average peak energy value between all three peak structures is calculated and stored as part of the same common peaks structure. The code required to implement this function is described in **Code 4.13.**

```
count = 0; //number of common peak structures identified
Threshold = 5; //peaks must be within five buckets of each other for each sensor
foreach (PeakStructure ps1 in PeakArray[0]) {  //ps1 = Sensor 1 Peak Structures
    foreach (PeakStructure ps2 in PeakArray[1]) {  // ps2 = Sensor 2 Peak Structures
        if (Math.Abs(ps1.Peak – ps2. Peak) <= Threshold) {
            foreach (PeakStructure ps3 in PeakArray[2]) {  // ps3 = Sensor 3 Peak Structures
                if (Math.Abs(ps1.Peak – ps3. Peak) <= Threshold) {
                    CommonPeaks[count].PeakStructure1 = ps1;
                    CommonPeaks[count].PeakStructure2 = ps2;
                    CommonPeaks[count].PeakStructure3 = ps3;
                    AverageEnergy = (ps1.Energy + ps2.Energy + ps3.Energy) / 3;
                    CommonPeaks[count].AverageEnergy = AverageEnergy;
                    CommonPeaks[count].AveragePeak = (ps1.Peak + ps2.Peak + ps3.Peak) / 3;
                    count = count + 1;
                }
            }
        }
    }
}
```

Code 4.13: Identify Common Peak Structures Function

As was done for the peak structures the common peaks array is sorted in

descending order based on the average peak energy value using the same bubble sorting

function described in **Code 4.12**. This sorting is done to allow the most relevant common

peak structure to be detected for a given energy range, and allow less relevant common

peaks structures in this same energy range to be discarded.

Once the array of common peak structures has been sorted, the average peak

bucket index value and average peak energy value of the peak structure is compared

against a criteria for detecting gamma sources. This criterion also specifies if the

minimum count requirements have been met for a confident detection by comparing the

average peak energy. These energy ranges and minimum peak energy counts for the

target gamma sources are described in **Table 4.3**.

Table 4.3: Minimum Peak Energy and Energy Ranges for Target Gamma Sources

Gamma Source	Bucket Range	Energy Range	Minimum Peak Energy
Barium[133]	69-91	306-406 keV	Greater than 2900
Cesium[137]	117-136	611-711 keV	Greater than 3500
Manganese[54]	144-162	784-884 keV	Greater than 1100
Cobalt[60]	191-208	1123-1223 keV	Greater than 1700
Unknown	Outside Identified Ranges		Greater than 1000

Each of the common peak structures is compared to the values in **Table 4.3**, and one of three following conclusions is made.

1. **Gamma Source Present**: The average peak bucket value falls within one of the gamma source energy ranges. This is classified as either a confident or not confident detection result if the peak energy meets the respective minimum count requirements for a gamma source.

2. **Unknown Source Present**: The average peak bucket value falls outside one of the gamma source energy ranges. This is classified as either a confident or not confident detection result if the peak energy meets the minimum count requirements for an unknown gamma source.

3. **Discard Result**: The average peak bucket value has already been identified by a common peak structure with a higher weight value.

The sensor has an assumed sensitivity range between $0 - 1.5 \text{MeV}$, and since each sensor has 256 buckets, one bucket index can equal an energy range between $4.4 - 5.8 \text{keV}$. Based on the GRDS characteristics the energy range increases as the bucket index increases. Therefore, a bucket index of 0 has an energy range of 4.4keV and a bucket index of 255 has an energy range of 5.8keV. Using **Table 4.3**, **Table 4.4** shows

the identification results of an example detection session and the common peaks

structures that were identified by the sensor array.

Table 4.4: Gamma Source Identification Results using a Sample Detection Session

Common Peaks Detected	Average Energy	Average Value		Detection Result	Gamma Source Detected
		Bucket	Energy		
Group 1	1200	42	177 keV	Confident	Unknown
Group 2	3864	80	360 keV	Confident	Barium[133]
Group 3	4443	126	656 keV	Confident	Cesium[137]
Group 4	3665	70	311 keV	Confident	Discarded
Group 5	599	199	1162 keV	Not Confident	Cobalt[60]

According to **Table 4.4,** *Group 2* and *Group 3* were identified because they fell

within a target energy range and met the minimum peak energy requirements. *Group 1*

fell within the minimum peak energy requirements, but did not fall within any target

energy range. *Group 2* fell in the same energy range as *Group 4*, but since *Group 4* had

lower or less relevant peak energy *Group 4* was discarded. *Group 5* fell within a target

energy range, but did not meet the minimum peak energy requirements.

4.2.8. Longitude Directional Determination

Once a common peaks group has been identified as a gamma source and a

confident detection result, a follow on phase is required to identify the longitude and

latitude direction. This is accomplished by fitting the activity ratios for each sensor's

peak energy with the curves described in the mathematical models for direction.

Therefore, the first step is to calculate the activity ratio for each sensor using **Equation

4.9**.

$$\text{ActivityRatio}_{Dx} = \frac{\text{PeakEnergy}_{Dx}}{\text{PeakEnergy}_{D1} + \text{PeakEnergy}_{D2} + \text{PeakEnergy}_{D3}}$$

Equation 4.9: Peak Energy Activity Ratio

The second step, using the previously evaluated directional models, involves quantifying a set of regions that describe the relationships between each sensors activity ratio and a set of longitude angle ranges. Since the configuration of the sensor array creates symmetry between $0 \leq \theta \leq 60°$, each region defines a 60 degree range between $0 \leq \theta < 360°$. In addition, each region defines an offset to be applied to the activity ratio fitting function for a given directional model curve. These 60 degree regions are defined in **Table 4.5**.

Table 4.5: Angle Region for Common Peaks Group Activity Ratio Values

Region	Energy Ratio Magnitude Comparison	Longitude Range
R1	$\text{ActivityRatio}_{D1} \geq \text{ActivityRatio}_{D3} \geq \text{ActivityRatio}_{D2}$	$0 \leq \theta \leq 60°$
R2	$\text{ActivityRatio}_{D1} \geq \text{ActivityRatio}_{D2} \geq \text{ActivityRatio}_{D3}$	$60 \leq \theta \leq 120°$
R3	$\text{ActivityRatio}_{D2} \geq \text{ActivityRatio}_{D1} \geq \text{ActivityRatio}_{D3}$	$120 \leq \theta \leq 180°$
R4	$\text{ActivityRatio}_{D2} \geq \text{ActivityRatio}_{D3} \geq \text{ActivityRatio}_{D1}$	$180 \leq \theta \leq 240°$
R5	$\text{ActivityRatio}_{D3} \geq \text{ActivityRatio}_{D2} \geq \text{ActivityRatio}_{D1}$	$240 \leq \theta \leq 300°$
R6	$\text{ActivityRatio}_{D3} \geq \text{ActivityRatio}_{D1} \geq \text{ActivityRatio}_{D2}$	$300 \leq \theta \leq 360°$

The values for the directional model curve are independently determined for each gamma source by collecting actual detection session datasets with the GRDS. Due to the symmetry of the sensor array, the datasets need to only include a range of source directions between $0 \leq \theta \leq 60°$. The number of datasets in this range is determined by a fixed degree interval. For example, if the fixed degree interval is 5 degrees, then the number of datasets would equal thirteen. To incorporate latitude detection, a set of the

same longitude angle datasets will be needed for gamma sources at different latitude
angles.

Each of the datasets would then need to be executed by the detection algorithm,
and the activity ratios would need to be calculated and recorded for each sensor and
gamma source [4]. These activity ratios define the directional model, and an example
output of this directional model is shown in **Table 4.6**.

Table 4.6: Longitude Directional Model for a Gamma Source

Sensor	Activity Ratios at 5° Intervals Between $0 \leq \theta \leq 60°$
D1	$AR_1 = \{410, 426, 451, 461, 485, 500, 519, 522, 528, 523, 518, 506, 502\}$
D2	$AR_2 = \{203, 189, 172, 167, 160, 155, 141, 141, 146, 170, 198, 230, 253\}$
D3	$AR_3 = \{385, 383, 375, 370, 353, 344, 338, 336, 325, 305, 282, 263, 243\}$

In both the software emulation tool and the GRDS computation system, **Table 4.6**
would be represented as a 3x13 matrix of values for each target gamma source and
latitude angle. To determine direction from this activity ratio matrix, a calculation is
completed based on **Table 4.5** to first determine the angle region. This angle region
result will establish three items for the fitting function.

1. Determine which of the three arrays the fitting function will compare with
   each sensor's calculated activity ratio, also known as array pairing.

2. Determine how the fitting function should index each activity ratio matrix.

3. Identify the angle offset to add to the resulting longitude angle of the fitting
   function.

Each of the thirteen element arrays in the ratio matrix will be either indexed
$0 \rightarrow 12$ or $12 \rightarrow 0$ based on the angle region that is determined. The activity ratio and

array pairing, along with the indexing scheme and offset for each angle region, is

described in **Table 4.7**.

Table 4.7: Activity Ratio Array Pairing, Indexing, and Offset for each Angle Region

Region	Activity Ratio 1	Activity Ratio 2	Activity Ratio 3	Offset
R1	$x \in AR_1 \mid$ x: $0 \to 12$	$x \in AR_3 \mid$ x: $0 \to 12$	$x \in AR_2 \mid$ x: $0 \to 12$	$+0°$
R2	$x \in AR_1 \mid$ x: $12 \to 0$	$x \in AR_2 \mid$ x: $12 \to 0$	$x \in AR_3 \mid$ x: $12 \to 0$	$+60°$
R3	$x \in AR_2 \mid$ x: $0 \to 12$	$x \in AR_1 \mid$ x: $0 \to 12$	$x \in AR_3 \mid$ x: $0 \to 12$	$+120°$
R4	$x \in AR_2 \mid$ x: $12 \to 0$	$x \in AR_3 \mid$ x: $12 \to 0$	$x \in AR_1 \mid$ x: $12 \to 0$	$+180°$
R5	$x \in AR_3 \mid$ x: $0 \to 12$	$x \in AR_2 \mid$ x: $0 \to 12$	$x \in AR_1 \mid$ x: $0 \to 12$	$+240°$
R6	$x \in AR_3 \mid$ x: $12 \to 0$	$x \in AR_1 \mid$ x: $12 \to 0$	$x \in AR_2 \mid$ x: $12 \to 0$	$+300°$

Based on the search rules outlined in **Table 4.5** and **Table 4.7**, a fitting function is

used to compare the mean square error (MSE) between the measured activity ratios for a

common peak structure and the directional model matrix. The code required to

implement this fitting function is described in **Code 4.14.**

```
if (IndexScheme = 0) {  //Regions R1, R3, R5
    for (int i = 0; i < 13; i++) {
        DeltaAR1 = AR1[ i ] – Ratio1;  //Ratio1 identified and set from pairing
        DeltaAR2 = AR2[ i ] – Ratio2;  //Ratio2 identified and set from pairing
        DeltaAR3 = AR3[ i ] – Ratio3;  //Ratio3 identified and set from pairing
        MSE = (DeltaAR1^2 + DeltaAR2^2 + DeltaAR3^2) / 3;
        if (MSE < MinimumMSE) {
            MinimumMSE = MSE;  //error
            IndexMSE = i;  //index
        }
    }
}
else if (IndexScheme = 1) {  //Regions R2, R4, R6
    for (int i = 0; i < 13; i++) {
        DeltaAR1 = AR1[12 - i] – Ratio1;  //Ratio1 identified and set from pairing
        DeltaAR2 = AR2[12 - i] – Ratio2;  //Ratio2 identified and set from pairing
        DeltaAR3 = AR3[12 - i] – Ratio3;  //Ratio3 identified and set from pairing
        MSE = (DeltaAR1^2 + DeltaAR2^2 + DeltaAR3^2) / 3;
        if (MSE < MinimumMSE) {
            MinimumMSE = MSE;  //error
            IndexMSE = i;  //index
        }
    }
}
```

Code 4.14: MSE Fitting Function

The index evaluated from **Code 4.14** represents the matrix index which resulted

in the smallest MSE and is concluded as the optimal search result from the fitting

function. This index, along with the offset identified from the angle region, is used in

conjunction with **Equation 4.10** to calculate the course angle.

$$\text{Course Angle } = \text{Offset} + (5 * \text{Index})$$

Equation 4.10: Gamma Source Course Angle Calculation

An example of an MSE calculation using the directional model described in

Table 4.6, and the activity ratios generated from a gamma source $\theta = 210°$, is illustrated

in **Figure 4.7**.
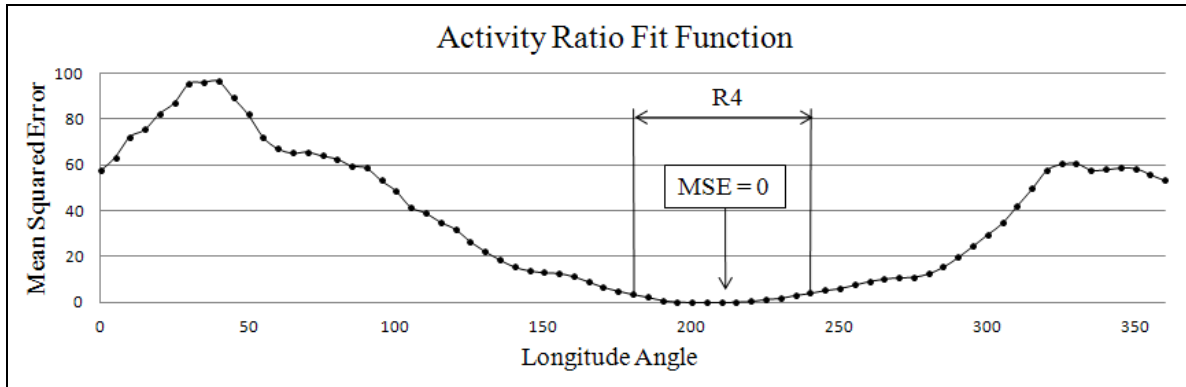
Figure 4.7: Mean Squared Error for Gamma Source @ $\theta = 210°$

Although **Figure 4.7** shows the MSE output for all longitude angles, the fitting function only needs to calculate MSE for a 60 degree range. This is because the angle region is already identified using **Table 4.5**, and in this example, the activity ratios would have fallen within region R4 according to **Table 4.5**. This means the offset for R4 is 180 degrees and the output of **Code 4.14** would produce an index value of 6 so that **Equation 4.10** would result in a longitude angle of $\theta = 210°$. In addition and most importantly, **Figure 4.7** illustrates that each longitude angle has a distinct MSE, and there is only one angle with a minimum MSE value.

In order to get to a finer granularity than 5 degrees, an additional MSE comparison can be done using the [Index + 1] and the [Index − 1] matrix values. Based on which of these index values have a smaller MSE a linear interpolation is performed to get the fine angle offset. **Equation 4.11** describes this fine angle calculation using the indexed MSE value and the course angle MSE value.

$$\text{Fine Angle}_{\text{Index}-1} = \text{Course Angle} - \left(5 * \frac{\text{MSE}_{\text{Course}}}{\text{MSE}_{\text{Index}-1}} \right)$$

$$\text{Fine Angle}_{\text{Index}+1} = \text{Course Angle} + \left(5 * \frac{\text{MSE}_{\text{Course}}}{\text{MSE}_{\text{Index}+1}} \right)$$

Equation 4.11: Gamma Source Fine Angle Calculation

A challenge arises for index values of 0 and 12, where the [Index − 1] or [Index + 1] value falls outside the standard directional model matrix. This requires an additional function which evaluates these activity ratio values directly based on the identified angle region. The look-up values for this function are described in **Table 4.8**.

Table 4.8: Indexing Activity Ratios outside the Directional Model Matrix

Region	AR Values [Index − 1], (Index = 0)			AR Values [Index + 1], (Index = 12)		
	Ratio1	**Ratio2**	**Ratio3**	**Ratio1**	**Ratio2**	**Ratio3**
R1	$AR_3[1]$	$AR_2[1]$	$AR_1[1]$	$AR_1[11]$	$AR_3[11]$	$AR_2[11]$
R2	$AR_1[11]$	$AR_2[11]$	$AR_3[11]$	$AR_3[1]$	$AR_1[1]$	$AR_2[1]$
R3	$AR_1[1]$	$AR_3[1]$	$AR_2[1]$	$AR_2[11]$	$AR_1[11]$	$AR_3[11]$
R4	$AR_3[11]$	$AR_1[11]$	$AR_2[11]$	$AR_2[1]$	$AR_3[1]$	$AR_1[1]$
R5	$AR_2[1]$	$AR_1[1]$	$AR_3[1]$	$AR_3[11]$	$AR_2[11]$	$AR_1[11]$
R6	$AR_2[11]$	$AR_3[11]$	$AR_1[11]$	$AR_1[1]$	$AR_2[1]$	$AR_3[1]$

The output of the fine angle calculation for each target source is the final longitude direction result for a given common peak group.

4.2.9. Latitude Directional Determination

This same process used to determine longitude direction is identical to the process for determining latitude direction. The primary difference is that instead of comparing one matrix for longitude and a given gamma source, there is an additional matrix required for each latitude angle. In addition, the following concerns exist for determining latitude direction.

1. Based on the fixed angle interval that is chosen for the latitude angle granularity, a 3x13 matrix is required for each interval.

2. The symmetry that was used for longitude directional determination can be less exploited in latitude directional determination. Instead of having six distinct regions that can be mathematically evaluated in the longitude angle, the latitude angles have two non-distinct regions.

3. The sensor array configuration has no method to evaluate if the gamma source is above or below the sensor, as per the amplitude compression model in **Figure 3.5**. The directional curve is identical between $0 \leq \phi \leq 90°$ and $360 \geq \phi \geq 270°$.

If a complete longitude and latitude directional model was developed using a fixed 5 degree interval it would take nineteen 3x13 matrixes for each target gamma source. The same MSE calculations would be done as in the longitude angle case, but now this needs to be done for each latitude matrix. This would create a total of 247 MSE values to calculate. In order to determine the fine angle offset the [Index-1] and [Index+1] activity ratios would need to be determined from adjacent latitude matrices versus adjacent values in the same longitude matrix.

Therefore, the additional computation time and the memory needed to store these matrices needs to be accommodated. If the GRDS does not have sufficient capabilities for this algorithm, then a specific latitude angle can be chosen to limit the number of matrices to store and calculate. Instead of providing a specific latitude angle result, this approach provides a general indication of the latitude angle.

Chapter 5: Results

The results for the isotope identification and detection algorithms were generated by programming the computation subsystem of the GRDS using the same algorithms that were defined and developed using the software emulation tool. Since there is no display output on the GRDS, the system was connected to a client PC through a universal serial bus (USB) interface. This connection allowed TeraTerm, a free software terminal emulator tool running on the PC, to communicate directly with the GRDS and both read and write data to the system. TeraTerm was used to program the algorithms to the computation subsystem, and also output each sensor's bucket data after a detection session had completed. In addition, this tool was used control the module by calling specific functions, and to display text based results.

5.1. GRDS Functions

To program the GRDS, the code developed with the software emulation tool had to be ported from C#, along with the activity ratio tables for each directional model, to C language. The primary challenge with this porting was that structures that were natively supported in C# had to be avoided in C language due to the limitations of the compiler. This required these structures to be implemented as a set of arrays with a fixed data type and tracked manually. In addition to this structure limitation, the NSP430 does not support floating point operations, and therefore all functions had to be examined to ensure rounding errors would not impede the results. All other functions and variables ported without issue due to both the algorithm design and the common baseline between C# and C language.

This ported code was then compiled using the GNU C compiler (GCC) tool into an NSP430 hex file. This hex file resulted in a codes space of 24kB where 2kB was required for calibration data, 6kB for variables, 1kB for activity ratios matrices, and 15kB was required for the algorithms. This binary was then flashed into the microcontroller memory over USB using TeraTerm. Once the flash was complete, the system was reset and enumerated into a development mode. This mode enabled each supported function to be called manually from TeraTerm and control each aspect of the detection sessions. In a production mode, this manual control would not be required and all functions would be called automatically by the GRDS based on detection event triggers. The isotope identification and source directional determination function execute in less than 100ms.

5.2. Dataset Collection

Once the GRDS is programmed, the first step was to determine the appropriate distance to place the sources and the time it would take to hit the minimum number of counts using the 1uCi sources. These parameters had to consider both the strength of the sources, the shadowing effects of the sensor array, and the near field and far field impacts. It was determined that a 10.0" source distance and a 5 minute collection time was appropriate to ensure the minimum number of counts was acquired to run the algorithms effectively. According to the mathematical models, any impacts from shadowing and near field effects would only impact directional determination, and would have minimal impact on isotope identification.

The GRDS program running in development mode has simple functions for controlling detection events and thereby enabling many datasets to be collected. In this mode, the system would automatically begin to capture gamma events and increment

each sensor's respective bucket counter after reset. Therefore, a function is available to clear all bucket values at any time. Calling this function would represent the start of a detection session and another function can be called to stop the detection session and output the bucket values.

To create a dataset, the target sources are placed at a distance of 10.0" from the center of the sensor array and set at a specific longitude and latitude angle. The function is called to clear the bucket values, and an independent timer is used to determine when 5 minutes had passed. At this point, the function would be called to read all the bucket values to the client PC. This hex output was then manually copied and pasted into a text file with the distance, longitude, and latitude angle listed in the file title.

Before collecting any data, the GRDS is activated with no sources in close proximity of the sensor array and let run for at least 30 minutes. This ensures all transients have settled before collecting any data. After this transient time, one measurement is taken with the gamma sources at one of the target directions to verify that the sensor is collecting data as expected. **Figure 5.1** shows a test output of the sensor array for Ba^{133}, Cs^{137}, Mn^{54}, and Co^{60}.
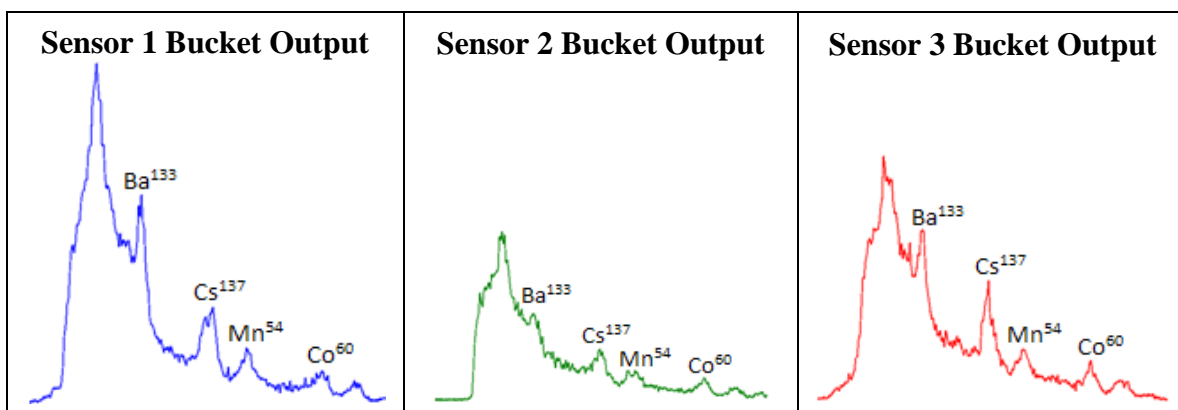

Figure 5.1: Test Output for Target Gamma Sources @ $\theta = 15°$, $\phi = 0°$

With the test output showing correct peak values at each of the source energy ranges, datasets can start to be collected. Per the mathematical model for longitude angle direction, datasets are needed from $0° \leq \theta \leq 60°$. Therefore, in 5 degree increments and at a latitude angle of $\phi = 0°$, datasets were collected with sources Ba^{133}, Cs^{137}, Mn^{54}, and Co^{60}. In order to add latitude determination, these datasets need to be taken again but with the sources at a different latitude angle. The latitude angle of $\phi = 45°$ was chosen as a midpoint between $0° \leq \phi \leq 90°$, but can be any value based on the latitude angles that need to be determined. These setups are illustrated in **Figure 5.2**.
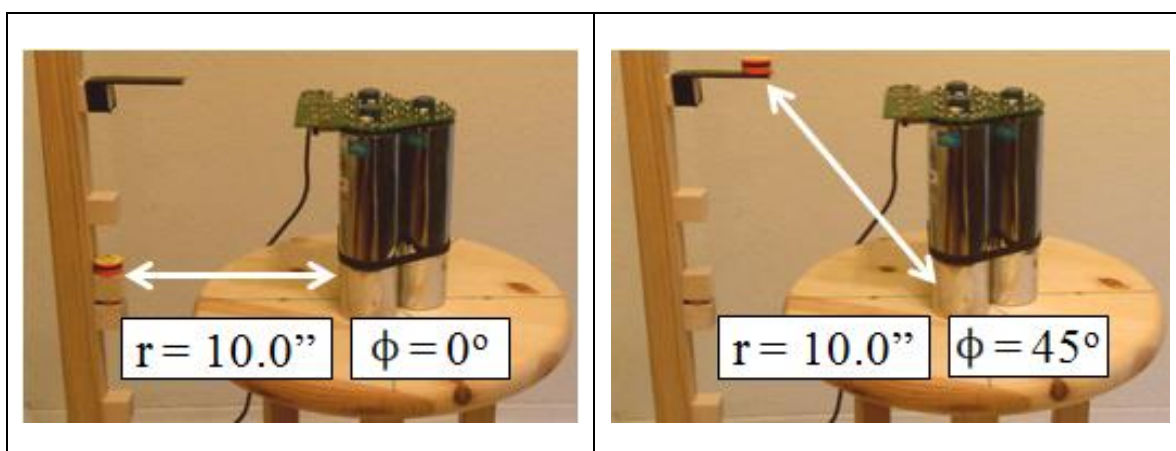
Figure 5.2: Setup for Collecting Directional Model Data

When taking these measurements, the gamma sources are stacked on top of each other with the highest energy source on the bottom. The reason the datasets for all four sources can be collected at the same time is because any interactions from sources at higher energy ranges will be removed during the offset energy calculations. In addition, the GRDS and detection algorithms should be able to determine isotope identity and direction for any source configurations that involves these four isotopes. This source stack configuration is illustrated in **Figure 5.3.**
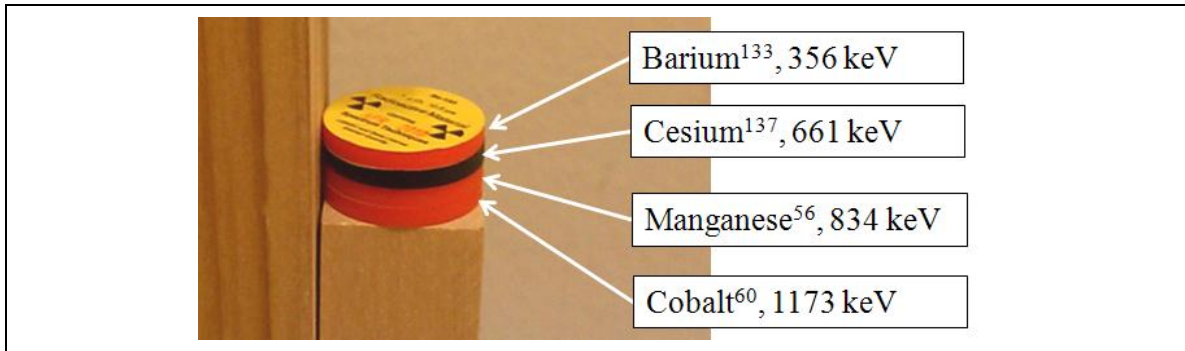
Figure 5.3: Source Stack Configuration

After the longitude measurements have been taken, there are thirteen datasets for each latitude angle for a total of 26 datasets. The sources then need to be placed below the sensor array at $\phi = 270°$ so a dataset can be generated for data calibration. This dataset will be used to set both the efficiency and alignment for the buckets of each sensor. Once the sources have been set, another 5 minute measurement is taken and the output is stored to another text file. This setup can be seen in **Figure 5.4**.
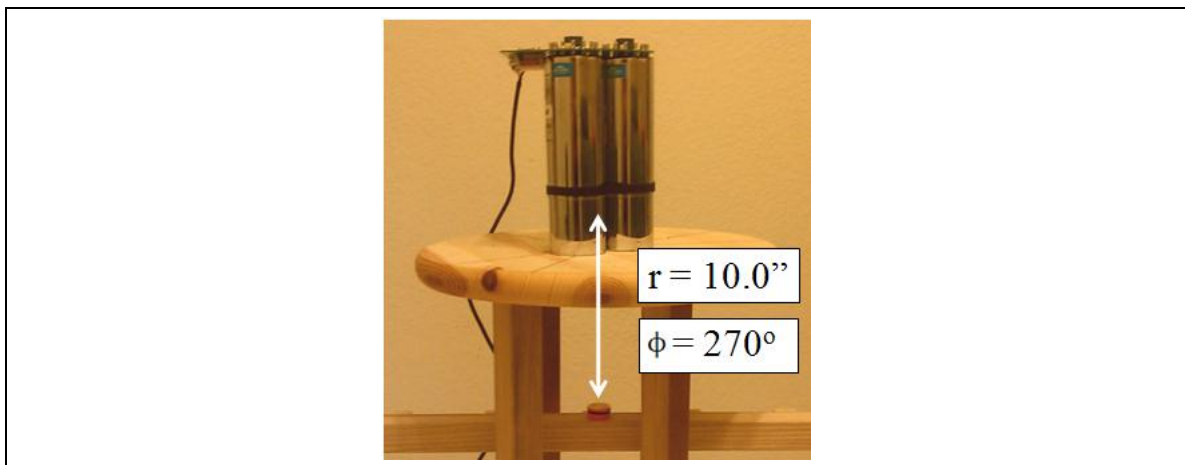
Figure 5.4: Test Setup for Efficiency

5.3.   Data Calibration

Data calibration is accomplished by loading the text file generated for both sensor alignment and efficiency in the software tool. This tool allows each of the calibration areas to be evaluated and adjusted. The data alignment value for each target energy range

is determined by inspecting the bucket value of each gamma source peak and for each

sensor. Based on the misalignment, a bucket shift value and energy range is identified

and assigned for each gamma source peak and sensor. The efficiency value for each

target energy range is determined using the course correction function and fine tuning

identities for each sensor. Based on the mismatch, a value relative to 256 is assigned to

each bucket which will compress or extend the peaks. As an example, an application of

the alignment and efficiency values are illustrated in **Figure 5.5** for a Cesium^{137} energy

peak.
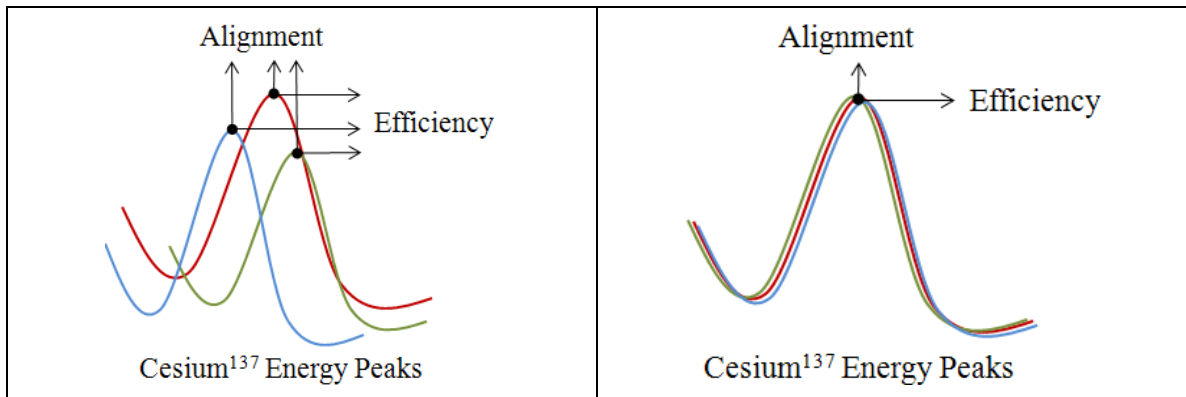
Figure 5.5: GRDS Efficiency and Alignment Before and After Data Calibration

The values determined for alignment and efficiency, along with values defined for

DNL offsets are then saved as a set of array values to be incorporated in the data

calibration algorithms. Once implemented, these values are then used to evaluate the

collected datasets for determining the directional models for each gamma source.

5.4.   Directional Models

Each of the datasets for each latitude angle are loaded into the software tool and

processed by the same algorithms which would be used by the GRDS computation

subsystem. Based on these results, the tool outputs the activity ratios for each target

gamma source and longitude angle between $0° \leq \theta \leq 60°$. These thirteen activity ratios

for each source represent the directional model for one latitude angle.

The software tool then takes these activity ratios and parses them based on the

symmetry of the sensor array and the identities for each angle region to create a full

directional data plot for $0° \leq \theta \leq 360°$. Although this full plot is not needed by the

directional determination algorithms, these values can be plotted to provide a full visual

confirmation of the stability of the model. A stable directional model should have

distinct values for each longitude angle, and should have smooth transitions between each

5 degree interval. This provides confidence that the fitting function can accurately

identify the correct activity ratio set. **Figure 5.6** shows examples of both a stable

directional model and an unstable directional model.
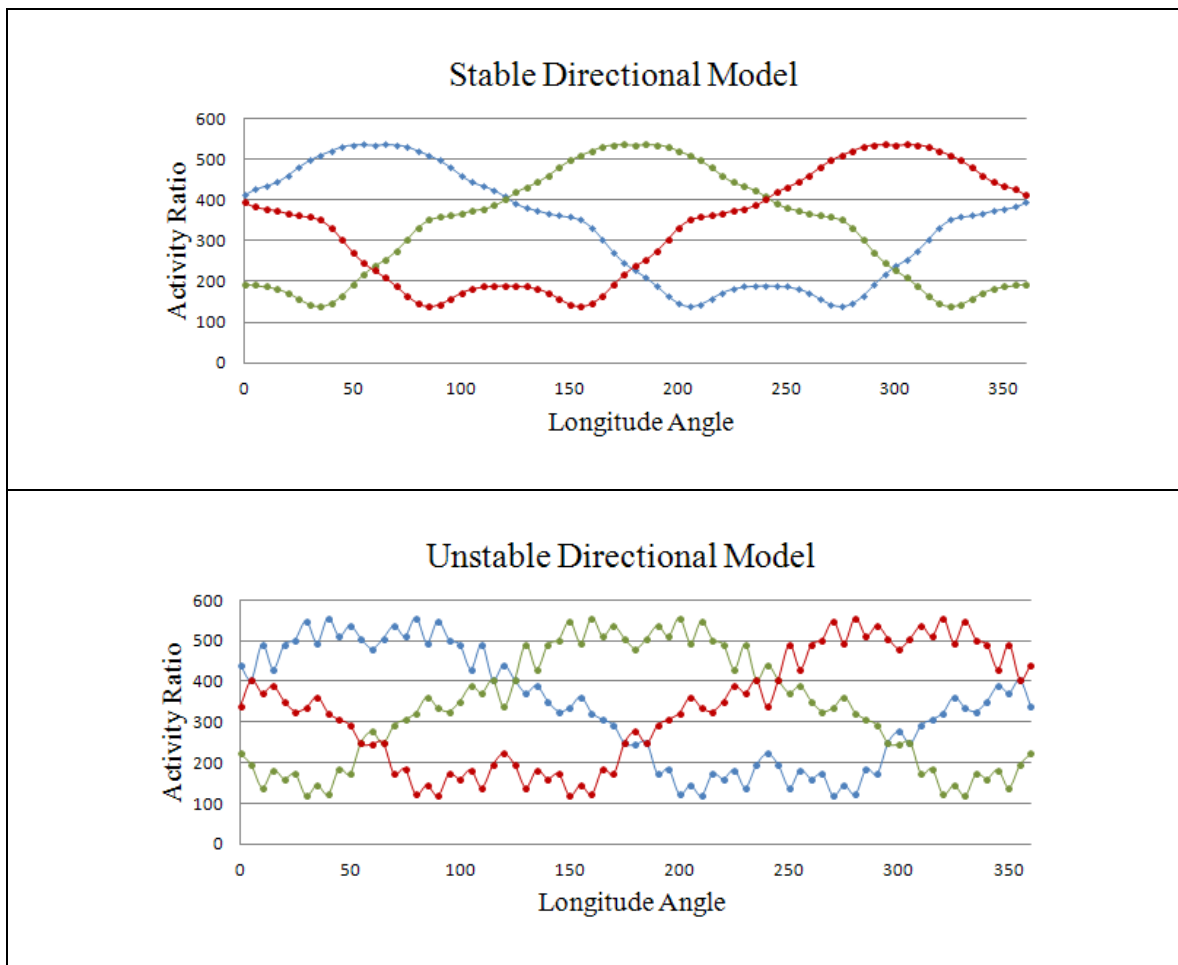
Figure 5.6: Stable and Unstable Directional Model Comparison

After concluding that the directional models are stable, the matrices are loaded

back into the software tool, and the same algorithms are run again against the datasets for

both latitude angles. The tool should output the correct isotope identification and

directional determination result for each dataset. If there are any issues with these results,

either the algorithms or directional models need to be adjusted until the results are

acceptable.

Once the directional models have been validated, the algorithms are ported to C

code, compiled by GCC, and then flashed into the NSP430 memory. To test the

algorithms the same process that was used for collecting model datasets is used, except

that instead of calling the TeraTerm function for dumping the bucket values, a new

function is called which processes the bucket values and outputs the identification and

directional results. During these test runs each of the four gamma sources are placed at a

distance of 10.0" and placed anywhere between $0° \leq \theta < 360°$ and either at $\phi =$

$0°$ or $\phi = 45°$. After the function is called, the final results are calculated, transmitted to

the client PC over USB, and then displayed using the TeraTerm prompt.

5.5.   Evaluating Results with the GRDS

Using the data collected for the four gamma sources, both the alignment attributes

and directional models are determined using the software emulation program. The data

calibration text file is first loaded into the tool to determine the GRDS efficiency and

alignment offsets. By comparing the peaks and the target source energy ranges for each

sensor, a relative value to 256 is assigned for efficiency and a shift value is assigned for

data alignment. As an additional check for efficiency, the identities described in **Table

4.1** are also compared against the longitude angles for each sensor at 0, 30, and 60

degrees. The data calibration results are described in **Table 5.1**.

Table 5.1: Calibration Data Results

Calibration Data	Sensor	Barium^{133}	Cesium^{137}	Manganese^{54}	Cobalt^{60}
Bucket Range	All	70-101	113-139	140-165	188-212
Sensor Efficiency Min-Max Ranges	D1	274-306	277-336	281-321	305-362
	D2	256-271	256-280	256-259	256-268
	D3	256-260	260-272	261-273	256-304
Data Alignment	D1	Bucket + 0	Bucket + 10	Bucket + 16	Bucket + 21
	D2	Bucket + 0	Bucket + 0	Bucket + 5	Bucket + 5
	D3	Bucket − 0	Bucket + 4	Bucket + 7	Bucket + 12

The values in **Table 5.1** for sensor efficiency are included in the efficiency matrix for each sensor. The bucket range value determines which indexes in the matrix to set the respective efficiency value. All other values in the matrix are set to 256 so that no calibration is done on those buckets. The data alignment value and bucket range is used to create an alignment set for each gamma source energy range.

To determine the directional model, the software tool loads the thirteen directional datasets for each latitude angle and calculates the activity ratios for each target gamma source between $0° \leq \theta \leq 60°$. Since there are four target gamma sources, and two latitude angles, this creates eight directional model matrices. To validate whether these directional models are stable, the activity ratio identities described in **Table 4.7** are used to calculate the remaining longitude values so the full directional model can be evaluated. These directional models are illustrated in **Table 5.2** through **Table 5.5** for each gamma source and each latitude angle.

Table 5.2: Longitude Directional Model Results for Barium^{133} @ ɸ=0°, ɸ=45°
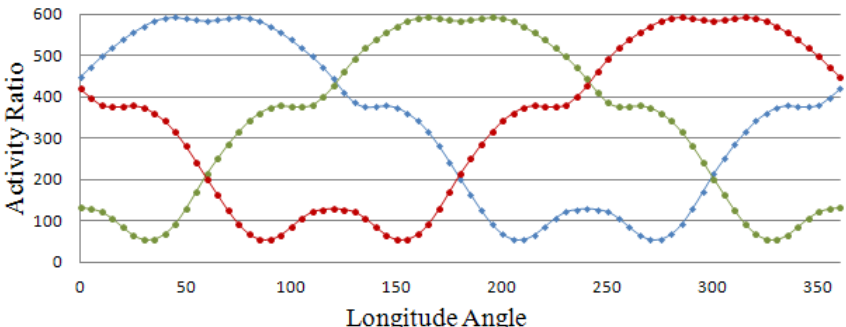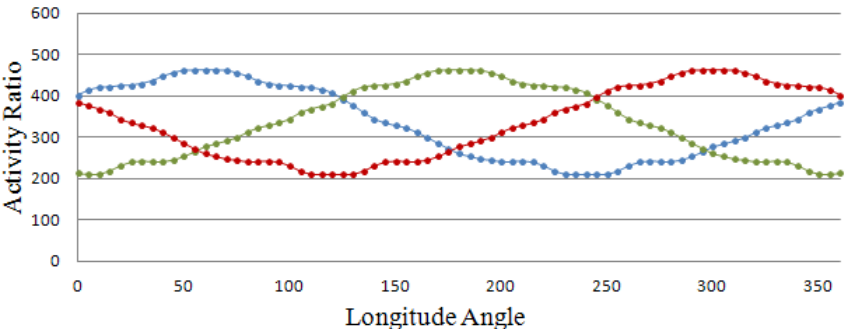
Barium^{133} Directional Model (ɸ = 0°)	**Max Value** 593.3 **Min Value** 54.2 **Amplitude** 539.1
Barium^{133} Directional Model (ɸ = 45°)	**Max Value** 462.5 **Min Value** 210.8 **Amplitude** 251.7

Table 5.3: Longitude Directional Model Results for Cesium[137] @ φ=0°, φ=45°
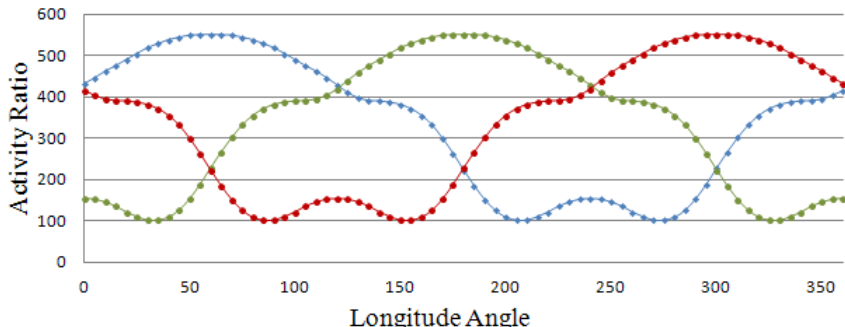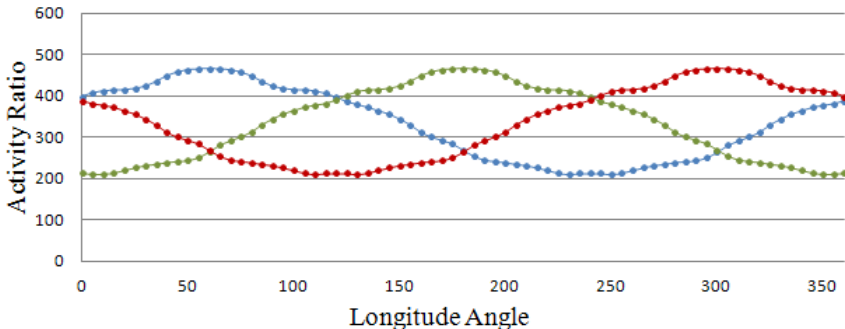
 Cesium[137] Directional Model (φ = 0°)	**Max Value** 550.2 **Min Value** 101.3 **Amplitude** 448.9
 Cesium[137] Directional Model (φ = 45°)	**Max Value** 466.2 **Min Value** 210.5 **Amplitude** 255.7

Table 5.4: Longitude Directional Model Results for Manganese[54] @ φ=0°, φ=45°

Manganese[54] Directional Model (φ = 0°)	**Max Value** 528.7 **Min Value** 141.3 **Amplitude** 387.4
Manganese[54] Directional Model (φ = 45°)	**Max Value** 466.2 **Min Value** 237.9 **Amplitude** 228.3

Table 5.5: Longitude Directional Model Results for Cobalt^{60} @ $\phi=0°$, $\phi=45°$
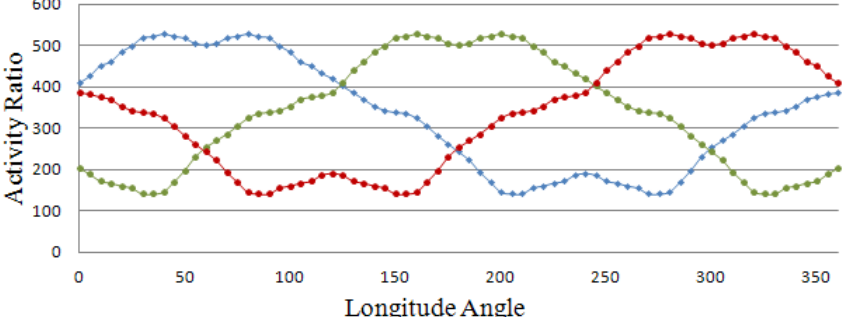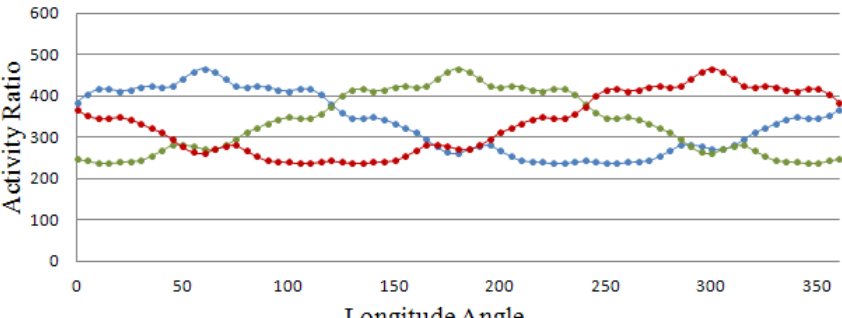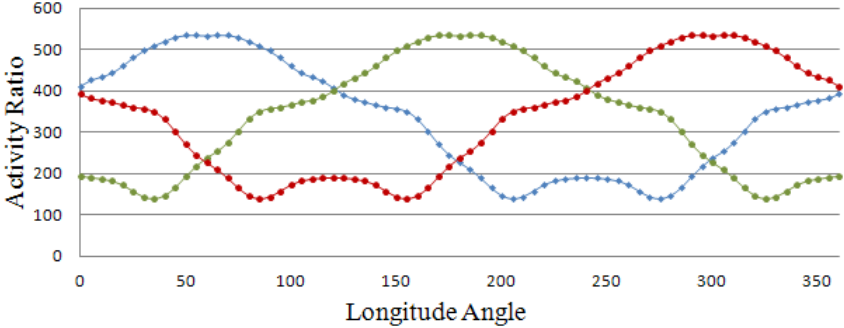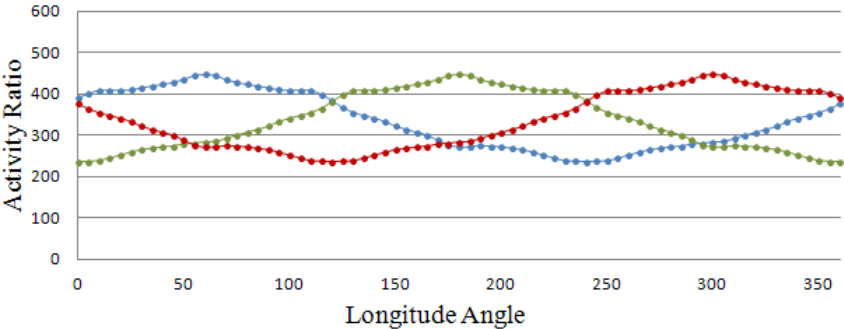
Cobalt^{60} Directional Model ($\phi = 0°$)	**Max Value** 536.1 **Min Value** 138.9 **Amplitude** 397.2
Cobalt^{60} Directional Model ($\phi = 45°$)	**Max Value** 446.8 **Min Value** 234.8 **Amplitude** 212.0

The relative structure of each directional model is similar for each gamma source and meets the criteria for a stable model as the curves are smooth and distinct for each longitude angle. Although the model structures are similar for each gamma source, the activity ratio values for each longitude angle and gamma source is distinct. Therefore, these tables illustrate the fact that a single directional model could not be developed for all sources, and that a separate directional model is needed for each gamma source.

Comparing the directional models for each gamma source, it is apparent that the amplitude value from the latitude angle $\phi = 45°$ is smaller than $\phi = 0°$. As described in the mathematical model for latitude angles, this is what is expected, and the amplitude value should trend to 0 as ϕ approach $\phi = 90°$. In addition, this key distinction in amplitude difference is what provides the ability for different latitude angles to be detected. An MSE comparison between each longitude model will yield a smaller error for the correct latitude angle.

Once the directional models have been evaluated, and there is confidence in the stability for each gamma source, the next step is to input the directional models into the detection algorithms. The software tool is then used to verify that for each dataset that each gamma source is identified and that both the longitude and latitude directions calculated is correct. After this is validated, these models are ported, compiled, and flashed in NSP430 code base and recompiled. The resulting binary is then flashed into the NSP430 memory.

Several different source configurations are chosen to determine how the algorithms will perform using the GRDS. This is important, since datasets were only collected and verified between $0 \leq \theta \leq 60°$, and all gamma sources were set to the same

fixed angle. Therefore, to test the symmetry assumption in the algorithms and verify the

overall functionality of the GRDS, test runs are completed with gamma sources at

different directions. Three test setups were chosen, each having a different gamma

source configuration with respect to the GRDS location. The three configurations are

based on 10.0" source distances and illustrated in **Figure 5.7** through **Figure 5.12**. For

each test setup, three test runs were evaluated by having the GRDS capture data for 5

minutes then calling the function to process the identification and directional

determination algorithms. The average results from the three test runs and for each setup

is described in **Table 5.6** through **Table 5.8**.
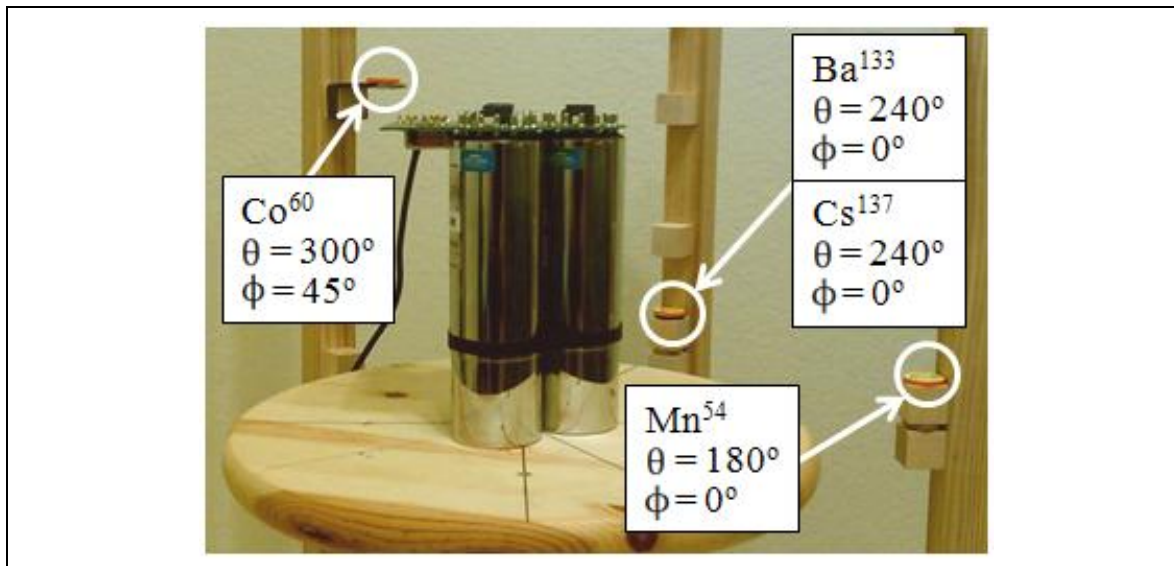
Figure 5.7: Setup 1 Gamma Source Configuration
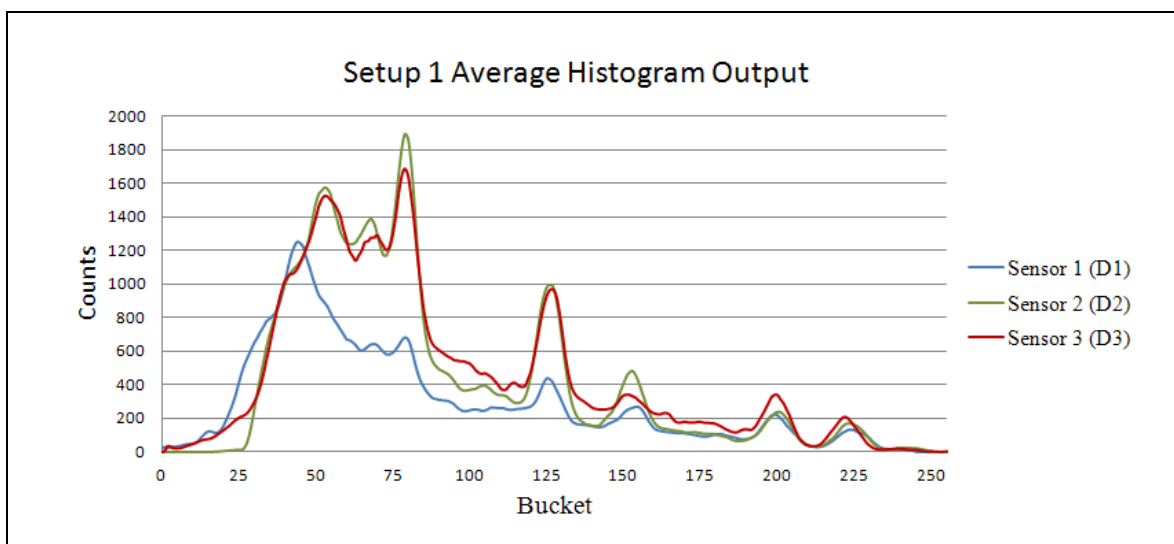
Figure 5.8: Setup 1 Average Histogram Output

Table 5.6: Average Results for Setup 1 Gamma Source Configuration

Test Run 1	Peak Energy	AR_{D1}	AR_{D2}	AR_{D3}	θ (Longitude)	ϕ (Latitude)
Barium^{133}	4874	102	473	425	232° (−8°)	0° (+0°)
Cesium^{137}	4407	150	481	369	229° (−11°)	0° (+0°)
Manganese^{137}	1655	251	528	222	178° (−2°)	0° (+0°)
Cobalt^{60}	1999	286	261	453	301° (+1°)	45° (+0°)
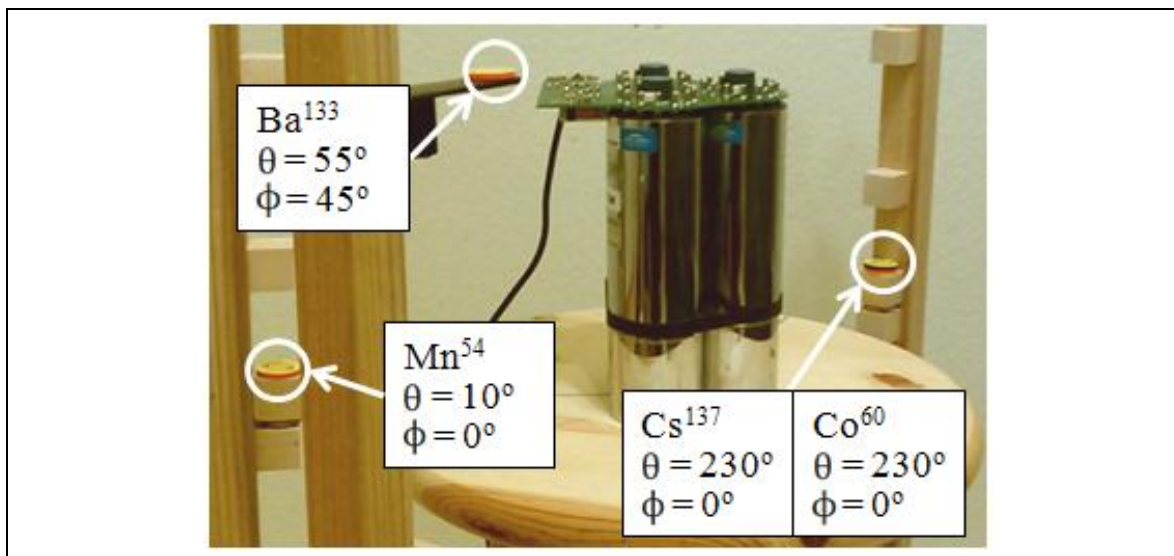
Figure 5.9: Setup 2 Gamma Source Configuration
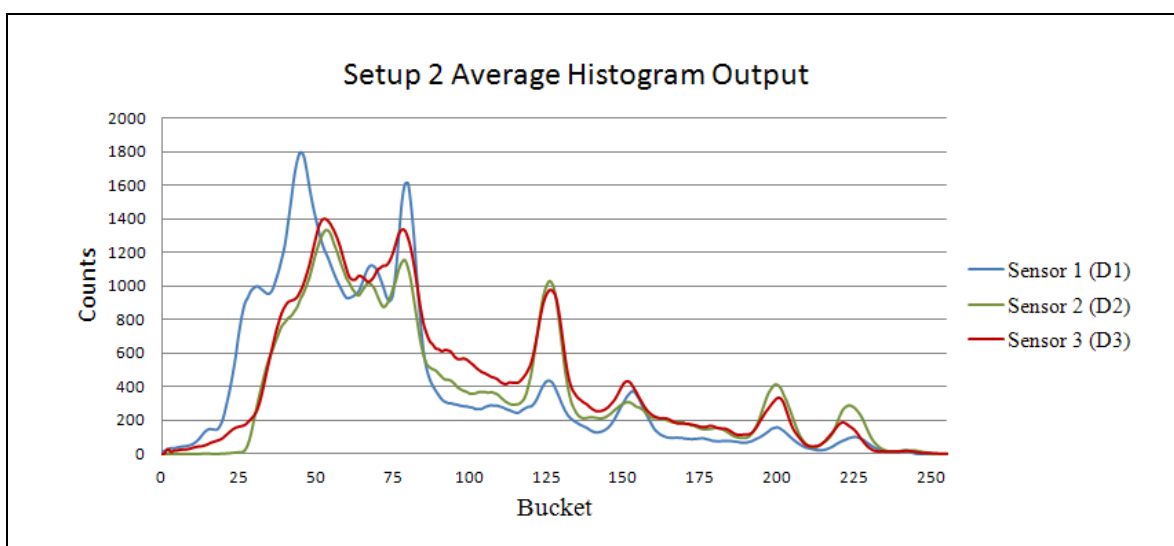
Figure 5.10: Setup 2 Average Histogram Output

Table 5.7: Average Results for Setup 2 Gamma Source Configuration

Test Run 2	Peak Energy	AR_{D1}	AR_{D2}	AR_{D3}	θ (Longitude)	ϕ (Latitude)
Barium[133]	4549	476	220	304	55° (+0°)	45° (+0°)
Cesium[137]	4387	153	476	371	230° (+0°)	0° (+0°)
Manganese[137]	1610	495	138	368	1° (−9°)	0° (+0°)
Cobalt[60]	2269	163	457	380	221° (−9°)	0° (+0°)
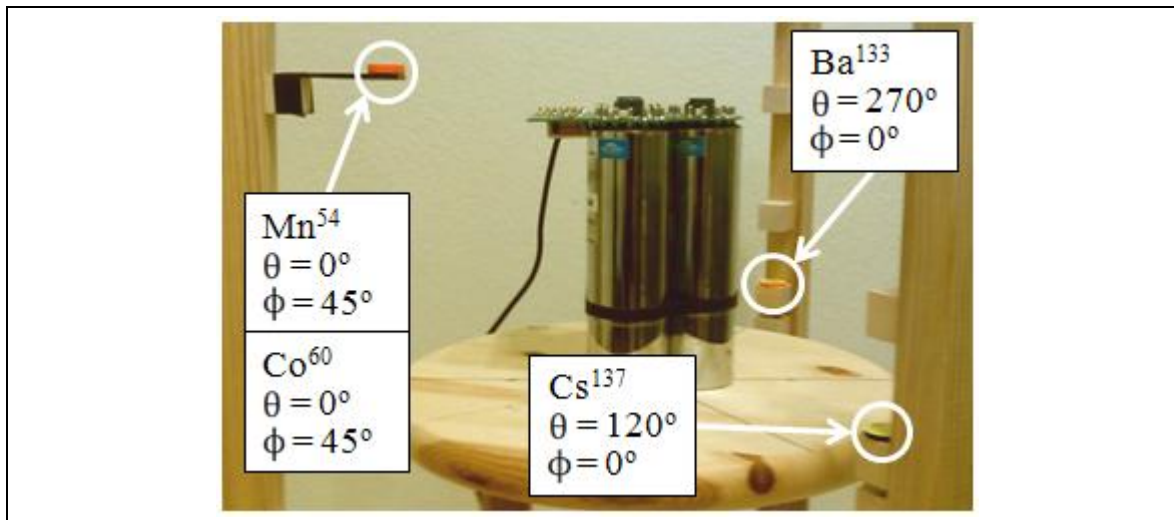
Figure 5.11: Setup 3 Gamma Source Configuration
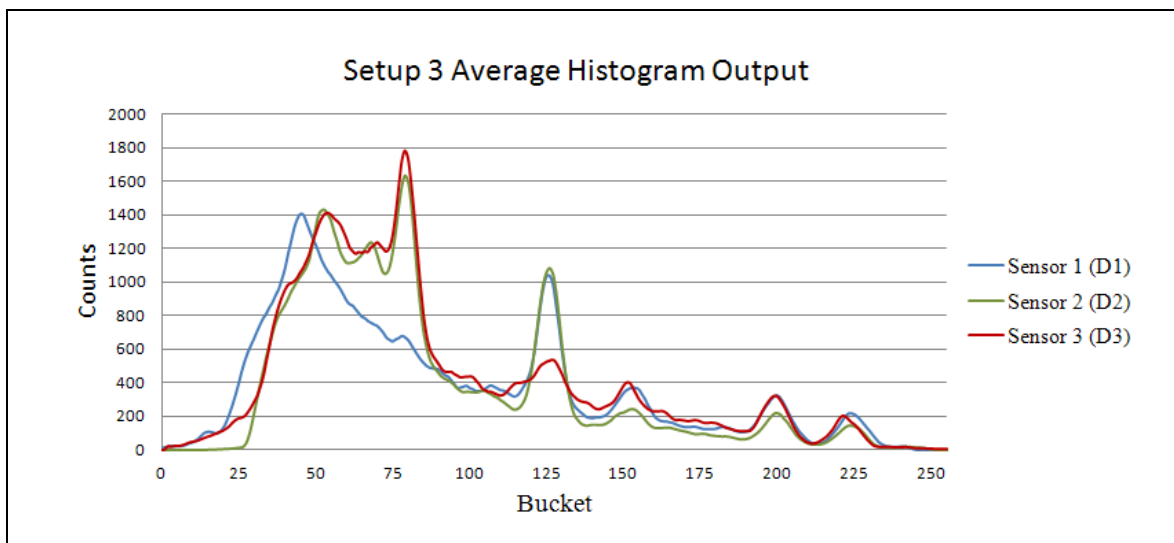
Figure 5.12: Setup 3 Average Histogram Output

Table 5.8: Average Results for Setup 3 Gamma Source Configuration

Test Run 3	Peak Energy	AR_{D1}	AR_{D2}	AR_{D3}	θ (Longitude)	ϕ (Latitude)
Barium^{133}	4439	42	418	539	267° (−3°)	0° (+0°)
Cesium^{137}	5170	422	454	124	124° (+4°)	0° (+0°)
Manganese^{137}	1368	479	177	344	12° (+12°)	45° (+0°)
Cobalt^{60}	2255	394	210	396	358° (−2°)	45° (+0°)

The results in **Table 5.6** through **Table 5.8**, along with additional test runs in the appendices show that for these three source configurations the algorithms identified the correct gamma source, the latitude angle direction, and the longitude angle direction within +/- 5% accuracy. Additional datasets can be taken to fully validate all different source directions and configurations, but these configurations provide an initial results baseline. These results also affirm that the respective algorithms provide accurate methods for gamma isotope identification and source directional determination.

Comparing the results that were calculated from the theoretical models to these measured results illustrate very distinct commonalities. The primary difference is that the calculated shadowing models assume a coefficient range between $0 \leq \tau \leq 100\%$, when the measured values show that the coefficient range limits should be higher than 0 and lower than 100. This is primarily due to the efficiency of the sensors and the gamma interactions that occur. This will result in gamma particles not always being absorbed by the crystal and therefore allowing a sensor that would otherwise be shielded to detect some of these particles. This explains why the activity ratio models do not have a trough value of zero.

Due to the weakness of the sources it was not possible to verify the differences between the near field and far field effects evaluated in the mathematical models. Therefore, only the near field models could be compared, but verifying the far field effects can be a focus for a future evaluation.

5.6.   Peak Energy Linearity

In addition to the identification and directional results, the average peak energy was measured at various time intervals. This was evaluated to determine how the peak

energy changes as exposure time increases and also how the counts varied between

different isotopes. The four target sources were placed at $\theta = 0°$, $\phi = 0°$ and

measurements were taken at 1 minute intervals between 0 and 5 minutes. The peak

energy outputs for these datasets are illustrated in **Figure 5.13**.
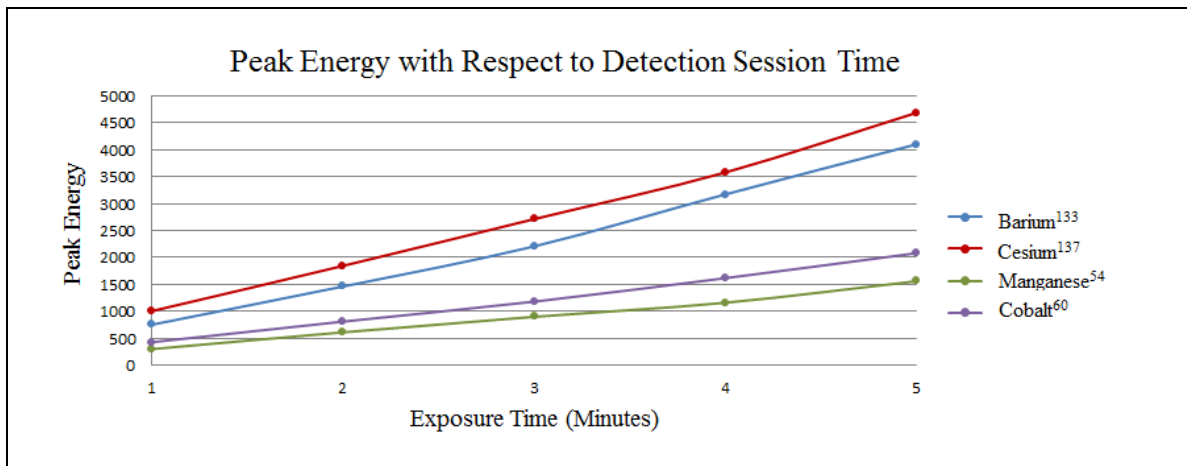
Figure 5.13: Counts with Respect to Detection Session Time

The graph in **Figure 5.13** reveals a linear distribution between average peak

energy and exposure time for each source. This also illustrates that the average peak

energy is different for each isotope, and justifies a minimum count value for each source.

This plot provides an additional mathematical model that could be utilized to provide

more detail about the sources. For example, if during a detection session the average

peak energy does not express a linear distribution, then this could reveal that the target

source is moving.

5.7.   GRDS Power Consumption

The power consumption of the GRDS is an important aspect of the detection

method design, because the system battery life must be suitable for a variety of industry

needs. The power consumption for the GRDS has been previously evaluated [2], and is

described in **Table 5.9**.

Table 5.9: GRDS Power Consumption

GRDS Power Component	Power Consumption
Processor Active Power	100-300uW/MHz
Processor Sleep Power	2.5 – 9.0uW
Crystal Oscillator, Biases, and References	3uW
Front End Power	$4 + 0.075 \times R$ uW/sensor $R = 1000$/s of particles/second
Crystal + PMT Sensor Array	0.5 – 1.0mW/sensor
Sensor Power Supply	20mW – 500mW/sensor

Based on the power management implemented as part of the GRDS, and the functions required to evaluate a detection session, the power can be evaluated as part of two modes and three phases. Each of the modes consists of a data monitoring, data collection, and data processing phase, but the modes differ depending on if the gamma event trigger mechanism is used or if the GRDS periodically measures the environment at a set time interval. The primary motivation for having two modes, based on a battery operation, depends on the efficiency of the supply used to power the sensors. If the supply is efficient, 20mW per sensor for example, then it may be acceptable to have the sensors running constantly, however if the sensor supply is not efficient, 500mW per sensor for example, then it may be more acceptable to periodically power the sensors and measure the environment at a set time interval. This decision primarily depends on the intended usage of the system.

The first phase is data monitoring. This phase is the default state of the GRDS and the computation subsystem will remain in a sleep state until either 12 gamma events have been captured or the system is woken up to take a periodic measurement. In this phase, the processor will remain in a sleep state and consume 2.5 – 9.0uW. The detector

subsystem will also consume power needed to operate both the sensors and the respective front end if the sensors are running constantly.

The second phase is data collection. This phase occurs once 12 gamma events have been captured or a periodic measurement is needed. The GRDS will then come out of a sleep state and constantly process the gamma events until either a timeout or a minimum number of counts have been reached. In this phase the processor will be in an active state and consume 100-300uW/MHz based on the processor clock, 3uW for the GRDS logic, along with the power to operate both the sensors and respective front end. If a specific timeout is implemented and this occurs before a minimum count occurs, then the GRDS will go back into a sleep state and the data monitoring phase will begin again.

The third phase is data processing. This phase occurs after the minimum number of counts has been reached, but also occurs in parallel with the data collection phase. This phase determines both when the minimum number of counts is reached, and also calculates the results for a detection session. If a number of counts is reached for a target energy range, the data collections stops, and the computational subsystem processes the results. Since the processor is in the active state, the system will consume 100-300uW/MHz, along with 3uW needed to drive the GRDS logic. Depending on the mode and if the sensors are still running, the power to operate both the sensors and the respective front end needs to be included.

Based on the datasets generated to create the directional models, and based on the strength of the gamma sources used, it is expected that a 5 minutes data session is required before the data can be processed. The average event count for 5 minutes and the four target sources at 10.0" was 300,000 which would equal to a front end power

consumption of 12-15uW for all three sensors. The power consumption by the supply for these three sensors would be 60mW for an efficient supply and 1.5W for an inefficient supply. If the processor is running at 60MHz, the data session would consume between 6-18mW for both data collecting and data processing. Once the results are generated the system goes back to a sleep state.

The battery life for the GRDS can be calculated using **Equation 5.1**. The battery life result is dependent on the percentage time required to collect and process a detection session along with the respective active state power consumption. This is used in conjunction with the battery capacity and the time the GRDS spends in a sleep state along with the respective sleep state power consumption.

$$\text{Battery Life} = \frac{\text{BatteryCapacity}}{(\text{ActivePower} \cdot \text{ActiveTime\%}) + (\text{SleepPower} \cdot \text{SleepTime\%})}$$

Equation 5.1: GRDS Power Consumption

Using **Equation 5.1**, **Table 5.10** compares the two detection modes when a detection session is triggered once every hour either through a periodic measurement or through the GRDS gamma event wake capability.   This would result in an active time rate of 8.3% and a sleep time rate of 91.6%. The GRDS is assumed to have a battery capacity of 1Whr.

Table 5.10: GRDS Power Consumption Mode Comparisons

Detection Mode	Sensor Supply	Active Power	Sleep Power	Battery Life
Periodic Measurement (1/hr)	Not Considered	21mW	12uW	569.6hrs
	Efficient Supply	81mW	12uW	148.5hrs
	Inefficient Supply	1.52W	12uW	7.9hrs
Gamma Event Detection	Not Considered	21mW	3mW	221.4hrs
	Efficient Supply	81mW	63mW	15.5hrs
	Inefficient Supply	1.52W	1.5W	0.7hrs

According to **Equation 5.1** and **Table 5.10** it is important to keep the GRDS in a sleep state as much as possible, which can be done by keeping the detection sessions minimal. This can be done either through a stronger gamma source, or allowing for a lower accuracy in the results by processing without reaching the minimum counts for a target energy range. This also emphasizes the importance of an efficient detector system optimized for power and that there is a trade-off between the strength of the source to be detected, accuracy of the results, and battery life.

Chapter 6: Conclusion

Gamma radiation can be utilized as either a productive tool when used with caution, or can be exploited to create a threat to society. In either case, the ability to proactively detect this radiation accurately will continue to be important for the safety of all individuals. Using a predefined gamma radiation detection system (GRDS), this thesis examined both theoretical models and actual methods to identify different gamma sources and their respective direction using this system.

Mathematical models were first examined and evaluated to provide a baseline understanding of gamma radiation and how it would be measured by the specific GRDS configuration. These models were then used as a key reference for developing algorithms that would process the gamma radiation profiles detected by the GRDS. These algorithms were first developed and validated on a client PC using a software emulation tool before being ported to the GRDS. This software tool allowed many detection sessions to be simulated and provided an environment that significantly helped to reduce development time. The algorithms were optimized to four target gamma sources, but could be scaled to implement more. A primary challenge however was the strength of the gamma sources that were used. This limited the distance at which the sources could be placed from the GRDS along with increase the time needed to reach the minimum number of counts for the algorithms.

The directional models that were measured by the GRDS closely represented the theoretical mathematical models that were calculated. These models create a tool which can be used to explore other sensor configurations and determine how gamma radiation would be measured. This tool also provides a model to determine near field and far field

effects for various gamma source distances. The directional models rely on a fitting function that searches for the matrix index which had the lowest mean squared error. This function exploits symmetry by evaluating a model which indexes 60 degrees versus 360 degrees to determine the source angular direction. Although not evaluated in this paper, there may be a more efficient model. It may be possible to create a single nonlinear function which maps all longitude and latitude angles to the activity ratios for each sensor. By inputting a set of activity ratios into the equation it could calculate both the longitude and latitude angle directly without having to evaluate a large number of matrices.

Data calibration was a key point discussed in this thesis as it is expected that every GRDS unit would need to be calibrated. This can be accomplished in software, as was the approach for this paper, or could be calibrated in hardware directly by assigning individual registers for efficiency and alignment. If accomplished through hardware the bucket data coming from each register would automatically be calibrated versus having to perform the calibration for each detection session.

There may be additional care required for gamma sources that have energy values within similar energy ranges. Based on the algorithm design, very distinct peaks are required for the algorithms to be most effective. This was not a problem for the target gamma sources since the energy ranges were far enough apart. However, if the peaks are not distinct for gamma sources with close energy ranges, this could create an issue for defining the energy offset values.

Based on the test cases that were run, and the validation completed using the software tool, the algorithms functioned correctly by identifying and determining the directions for each of the source configurations within +/-5% accuracy. Additional testing could be completed using different distances and additional longitude and latitude angles. However, due to the weakness of the sources, it created a fundamental limitation for testing far field distances. In order to collect the thirteen text files for each angle, and with the minimum counts needed for a given distance, the detection session time grows as distance increases. The only way to decrease this time is to use stronger sources, but then that creates a health concern for the tester. This is the primary reason why the distance of 10.0" was used, but should scale with stronger sources and further distances. In each intended usage case this accuracy value for a production system would need to be specified. Also, to ensure the GRDS system is low power, a timeout may be required so the system is not constantly collecting data until the minimum count thresholds are met. In addition, a future investigation could be done involving multiple GRDS units placed at fixed distances to determine not only direction, but also triangulate an exact position.

This thesis describes a series of methods for accurately identifying isotopes and then determining the respective longitude and latitude positions. These methods can continue to be refined and perfected to create a solid detection system based on the requirements needs for a given industry. This will ensure the safety of individuals for those industries requiring immediate and accurate knowledge of when, where, and how much gamma radiation may be present at any given time.

References

[1] ORTEC, "905 Series Nal(TI) Scintillation Detectors Data Sheet", 801 South Illinois Ave., Oak Ridge, TN 37831, http://www.ortec-online.com/download/905-Series-NaI(Tl)-Scintillation-Detectors.pdf, Retrieved 2011-07-23.

[2] N. Schemm, S. Balkır, M.W. Hoffman, et al., "A Single Chip Computational Sensor System for Neutron Detection Applications," IEEE Sensors Journal, vol. 10, no. 7, pp. 1226-1233, July 2010.

[3] Doug Reilly, Norbert Ensslh and Hastings Smith Jr., Sarah Kreine, Office of Nuclear Regulatory Research, U.S. Nuclear Regulatory Commission, Passive Nondestructive Assay of Nuclear Materials (PANDA), pp. 31-40, March 1991.

[4] N. Schemm, S. Balkır, M.W. Hoffman, M Bauer, "A Directional Gamma Ray Detector Using a Single Chip Computation Sensor.", IEEE Sensors 2011, Limerick, Ireland, October 2011

[5] N. Schemm, B. Liang, S. Balkır, M.W. Hoffman, M Bauer, "A Single Chip Computational Sensor System for Gamma Isotope Identification," IEEE Int. Symp. on Cir. and Sys. (ISCAS) 2010, pp. 2271-2274, Paris, June 2010.

Appendices

10 Second Detection Session - Sources @ 4.0"

Test Run	Peak Energy	AR_{D1}	AR_{D2}	AR_{D3}	θ (Longitude)	φ (Latitude)
Barium[133]	731	842	68	89	56° (−4°)	0° (+0°)

10 Second Detection Session - Sources @ 4.0"

Test Run	Peak Energy	AR_{D1}	AR_{D2}	AR_{D3}	θ (Longitude)	φ (Latitude)
Cesium[137]	730	772	117	110	61° (+1°)	0° (+0°)

10 Second Detection Session - Sources @ 4.0"

Test Run	Peak Energy	AR_{D1}	AR_{D2}	AR_{D3}	θ (Longitude)	φ (Latitude)
Manganese[137]	238	795	111	92	61° (+1°)	0° (+0°)

10 Second Detection Session - Sources @ 4.0"

Test Run	Peak Energy	AR_{D1}	AR_{D2}	AR_{D3}	θ (Longitude)	φ (Latitude)
Cobalt[60]	208	709	123	166	58° (−2°)	0° (+0°)

10 Second Detection Session - Sources @ 4.0"

Test Run	Peak Energy	AR_{D1}	AR_{D2}	AR_{D3}	θ (Longitude)	φ (Latitude)
Barium[133]	705	416	519	64	142° (+12°)	0° (+0°)
Cesium[137]	546	763	18	217	44° (+14°)	0° (+0°)
Manganese[137]	249	569	411	18	100° (−14°)	0° (+0°)
Cobalt[60]	283	698	217	83	69° (−1°)	0° (+0°)

10 Second Detection Session - Sources @ 4.0"

Test Run	Peak Energy	AR_{D1}	AR_{D2}	AR_{D3}	θ (Longitude)	φ (Latitude)
Barium[133]	869	445	48	506	334° (+6°)	0° (+0°)
Cesium[137]	692	115	812	71	179° (−1°)	0° (+0°)

10 Second Detection Session - Sources @ 4.0"

Test Run	Peak Energy	AR$_{D1}$	AR$_{D2}$	AR$_{D3}$	θ (Longitude)	φ (Latitude)
Barium^{133}	521	22	658	318	198° (−12°)	0° (+0°)
Manganese^{137}	148	210	170	618	302° (+2°)	0° (+0°)

10 Second Detection Session - Sources @ 4.0"

Test Run	Peak Energy	AR$_{D1}$	AR$_{D2}$	AR$_{D3}$	θ (Longitude)	φ (Latitude)
Barium^{133}	724	666	320	13	79° (+11°)	0° (+0°)
Cesium^{137}	675	444	478	76	133° (+13°)	0° (+0°)
Manganese^{137}	195	736	133	129	61° (+1°)	0° (+0°)

2 Minute Detection Session - Sources @ 10.0"

Test Run	Peak Energy	AR$_{D1}$	AR$_{D2}$	AR$_{D3}$	θ (Longitude)	φ (Latitude)
Barium^{133}	1764	259	263	477	300° (+0°)	45° (+0°)
Cesium^{137}	1507	282	277	439	304° (+4°)	45° (+0°)
Manganese^{137}	450	285	278	463	309° (+9°)	45° (+0°)
Cobalt^{60}	656	267	288	444	297° (−3°)	45° (+0°)

2 Minute Detection Session - Sources @ 10.0"

Test Run	Peak Energy	AR$_{D1}$	AR$_{D2}$	AR$_{D3}$	θ (Longitude)	φ (Latitude)
Barium^{133}	1560	206	575	217	180° (+0°)	0° (+0°)
Cesium^{137}	1521	232	561	205	180° (+0°)	0° (+0°)
Manganese^{137}	470	220	613	165	178° (−2°)	0° (+0°)
Cobalt^{60}	819	244	527	227	180° (+0°)	0° (+0°)

2 Minute Detection Session - Sources @ 10.0"

Test Run	Peak Energy	AR_{D1}	AR_{D2}	AR_{D3}	θ (Longitude)	ϕ (Latitude)
Barium[133]	2297	430	437	132	121° (+0°)	0° (+0°)
Cesium[137]	2165	429	423	147	116° (+0°)	0° (+0°)
Manganese[137]	838	614	86	299	41° (+11°)	0° (+0°)
Cobalt[60]	545	210	370	418	257° (−13°)	45° (+0°)

2 Minute Detection Session - Sources @ 10.0"

Test Run	Peak Energy	AR_{D1}	AR_{D2}	AR_{D3}	θ (Longitude)	ϕ (Latitude)
Barium[133]	1596	280	263	456	300° (+0°)	45° (+0°)
Cesium[137]	1448	205	596	197	181° (+1°)	0° (+0°)
Manganese[137]	651	396	458	144	124° (+4°)	0° (+0°)
Cobalt[60]	811	396	458	144	177° (−3°)	0° (+0°)

2 Minute Detection Session - Sources @ 10.0"

Test Run	Peak Energy	AR_{D1}	AR_{D2}	AR_{D3}	θ (Longitude)	ϕ (Latitude)
Barium[133]	1688	455	414	130	117° (−3°)	0° (+0°)
Cesium[137]	1208	258	343	398	271° (+1°)	45° (+0°)
Manganese[137]	369	558	61	380	31° (+1°)	0° (+0°)
Cobalt[60]	670	210	343	398	256° (−14°)	45° (+0°)

5 Minute Detection Session - Sources @ 24.0"

Test Run	Peak Energy	AR_{D1}	AR_{D2}	AR_{D3}	θ (Longitude)	ϕ (Latitude)
Barium[133]	695	66	506	427	221° (+11°)	0° (+0°)